Validation of the software package IMD for molecular dynamics simulations of laser induced ablation for micro propulsion

Wissenschaftliche Arbeit zum ersten Staatsexamen

Institute for Theoretical and Applied Physics,
University of Stuttgart
in cooperation with the Institute of Technical Physics,
German Aerospace Center (DLR)

vorgelegt von: Daniel J. Förster
Gutachter: PD Dr. Johannes Roth
Betreuer am DLR: Dr. Stefan Scharring
Vorgelegt am: 20. Juni 2013

Erklärung der Selbständigkeit

Ich erkläre, dass ich die Arbeit selbständig angefertigt und nur die angegebenen Hilfsmittel benutzt habe. Alle Stellen, die dem Wortlaut oder dem Sinn nach anderen Werken, gegebenenfalls auch elektronischen Medien, entnommen sind, sind von mir durch Angabe der Quelle als Entlehnung kenntlich gemacht. Entlehnungen aus dem Internet sind durch Angabe der Quelle und des Zugriffsdatums sowie dem Ausdruck der ersten Seite belegt; sie liegen zudem für den Zeitraum von 2 Jahren entweder auf einem elektronischen Speichermedium im PDF-Format oder in gedruckter Form vor.

Im Falle der Aufbewahrung meiner Arbeit erkläre ich mein Einverständnis, dass die Arbeit zugänglich gemacht wird.

Stuttgart, den 20. Juni 2013

Daniel Johannes Förster

Daniel J. Förster

Acknowledgement

I would like to offer my special thanks to my university advisor PD Dr. Johannes Roth for his valuable and constructive suggestions during the planning and development of this research work. I also would like to thank Dr. Stefan Scharring for support and scientific inputs and discussions of all kind.

Prof. Dr. Hans-Rainer Trebin and PD Dr. Adolf Gießen for admitting me to their institutes and making me feel very welcome on both sides of the street, i.e. ITAP and ITP.

Also I want to thank Mr. Alexander Kiselev and Mr. Jan Lotze at ITAP for fruitful discussions on laser ablation simulations and parallel processing.

Furthermore I want to thank the group of Dr. Hans-Albert Eckel at DLR, the working atmosphere always was good and inspiring. Thanks to Ms. Stefanie Karg and Mr. Johannes Peter.

Mr. Jan Meisner for dialogs on quantum chemistry, as well as getting another point of view on the topic.

Finally, I want to thank my family and friends for support over the last years.

Daniel J. Förster

Zusammenfassung in deutscher Sprache

Das Konzept für einen Mikroantrieb auf Basis von Laserablation (MICROLAS) des Instituts für Technische Physik (ITP) des DLR Stuttgart stellt eine mögliche Alternative zu bestehenden Konzepten im $\mu N - \mu N$-Bereich dar. Es basiert auf Laserablation, also dem Materialabtrag bei Bestrahlung eines Targets mit einem gepulsten Laser. Die Möglichkeit zur genauen Regelung der eingetragenen Energie durch den Laser sowie dessen Repetitionsrate sollte zu regelbarem Materialabtrag führen, der in einem weiten Bereich von genau einstellbaren Impulsbits resultieren kann. Die Genauigkeit, technische Machbarkeit sowie Reproduzierbarkeit wird und wurde in einer Reihe von Studien am ITP geprüft. In der vorliegenden Arbeit wird das Programm IMD des Instituts für Theoretische und Angewandte Physik (ITAP) der Universität Stuttgart zur Simulation des Materialabtrages diskutiert. Durch Skripte werden aus den Daten des Programms wichtige Parameter extrahiert und für ein weiteres Programm bereitgestellt, das die zeitliche Entwicklung des Ablationsjets simulieren soll (PICLas Code). Die Ergebnisse der durchgeführten Simulationen werden mit solchen eines hydrodynamischen Simulationsprogramms (VLL) sowie mit experimentellen Daten verglichen.

Daniel J. Förster

Abstract

A new concept of micro propulsion based upon laser ablation was introduced by the Institute of Technical Physics of DLR Stuttgart. Pulsed lasers are used for material removal of a target. The amount of removed material should be tuneable due to the tuneability of input laser energy and repetition rate, resulting in well defined impulse bits and low small thrusts down to the sub-μN scale. Its accuracy, feasibility and reproducibility were and still are under examination.

In this thesis, the program IMD of the Institute of Theoretical and Applied Physics is discussed with respect to the simulation of ablation. Via scripts, data output of the program is converted into important parameters and provided for another program intended for simulation of the ablation jet (PICLas code). Results of executed simulations are compared with those of a hydrodynamic simulation program (VLL) and experimental data.

Daniel J. Förster

Glossary

Conventions in this thesis

Scalar values as the wavelength, time or frequency are presented in standard text format like

$$\lambda, t, \nu,$$

whereas vectors like coordinates in space or forces are printed bold, e.g.

$$\mathbf{r}, \mathbf{F}.$$

If in not declared otherwise, units are of the SI-system and vectors exhibit three real components. If scalar values appear that have a vectorial equivalent, usually their absolute value is meant, i.e. $a = |\mathbf{a}| = \left|\left(a_1\ ,\ a_2\ ,\ a_3\right)^T\right| = \sqrt{\sum_{i=1}^{3}\ a_i^2}$.

Abbreviations

CW	Continuous wave
DFT	Density functional theory
DLR	German aerospace center
DSMC	Direct simulation Monte Carlo
EAM	Embedded atom model
fcc	face centered cubic
FD	Finite difference
FWHM	Full width half maximum
IMD	ITAP Molecular Dynamics
ITAP	Institute of Theoretical and Applied Physics
ITP	Institute of Technical Physics
MD	Molecular Dynamics

NVE	Ensemble with constant particle number, volume and energy
NVT	Ensemble with constant particle number, volume and temperature
PIC	Particle in cell
RES	Rescaling
TTM	Two temperature model
VLL	Virtual laser lab

Conversion rules between IMD and SI units

quantity	definition	transformation IMD $\leftrightarrow$ SI units
energy E		$1\ eV = 1.60217733 \cdot 10^{-19}$ J
location x		$1\ \text{Å} = 10^{-10}$ m
mass m		$1\ amu = 1.660538 \cdot 10^{-27}$ kg
time t	$[t] = \sqrt{\frac{[m]\ [x]^2}{[E]}}$	$1\ \mathrm{IMDu}(t) = 10.1806 \cdot 10^{-15}$ s
temperature T	$[T] = \frac{3}{2}\frac{[E]}{[k_B]}$	$1\ \frac{eV}{k_B} = 1.60217733 \cdot 10^{-19}\ \frac{J}{k_B} \approxeq 11605$ K
pressure p	$[p] = \frac{[m]}{[x]\ [t^2]}$	$1\ \mathrm{IMDu}(p) \approx 1.60222 \cdot 10^{11}$ Pa
electron-phonon coupling parameter G	$[G] = \frac{[E]}{[t]\ [x^3]\ [T]}$	$1\ \mathrm{IMDu}(G) \approx 1.3561 \cdot 10^{21}\ \frac{J}{s\ m^3\ K}$
heat capacity C	$[C] = \frac{[E]}{[x^3]\ [T]}$	$1\ \mathrm{IMDu}(C) \approx 1.3806 \cdot 10^{7}\ \frac{J}{m^3\ K}$
thermal conductivity K	$[K] = \frac{[E]}{[x]\ [t]\ [T]}$	$1\ \mathrm{IMDu}(K) \approx 13.561\ \frac{J}{s\ K\ m}$
proportional coefficient γ	$[\gamma] = \frac{[C]}{[T]}$	$1\ \mathrm{IMDu}(\gamma) \approx 1189.7\ \frac{J}{m^3\ K^2}$
fluence Φ	$[\Phi] = \frac{[E]}{[x^2]}$	$1\ \frac{eV}{Å^2} \approx 16.022\ \frac{J}{m^2}$

Contents

1. Introduction

Within the past few years projects in earth and space exploration were planned with the need for very precise position control systems not available yet. The forces acting on satellites have to be compensated accurately. Existing thrusters have problems of endurable precise regulation of thrusts down to a few μN. Examples are chemical engines like hydrazine boosters, pulsed plasma thrusters or arcjets. An alternative to existing concepts in $nN - \mu N$ regime like nano-FEEPs, MEMS-ion thrusters or HEMP thrusters was introduced by the Institute of Technical Physics (ITP) of DLR Stuttgart [1]. It is based upon laser ablation of a (solid) propellant material and in the future shall guarantee position control of pretentiously missions like LISA Pathfinder [2] or MICROSCOPE [3].

Laser ablation has been studied within the last decades, many groups in the meanwhile are active in this field. At the Institute for Theoretical and Applied Physics (ITAP) at the University of Stuttgart ultrashort pulses in the fs-regime have been investigated through simulations. An existing Molecular Dynamics code of the institute, IMD, was under further development to enable the simulation of pulsed laser ablation [4]. This thesis investigates on the validation of IMD for calculations in the aerospace field.

At ITP the first estimations on aerospace parameters are done amongst others with a hydrodynamic model, VLL. It is a web tool that offers one dimensional simulations of laser ablation simulations for a few materials. Comparison of the output of both programs, IMD and VLL, is of interest, since the simulation times differ significantly from each other.

At the DLR facility in Stuttgart, laser ablation experiments were and are under development. Partially, the measurement of important quantities such as impulse coupling coefficient, specific impulse and angle distributions of neutral and charged particles were performed. Data of these will be compared with both simulation programs.

The structure of this thesis is of the following order. First, the concept of the new thruster is explained, also an introduction in theory on solid state physics, lasers and laser ablation is given. In the next chapter, the models used in simulations are introduced, as well as comments on the implementation of IMD are given. Chapter 4 describes the developments and results obtained from working on this project. Finally, conclusions are made and suggestions for future developments are given.

2. Theory

In this part of the work theoretical background is provided. The first section illustrates the concept of the **MICROLAS propulsion** being developed at the Institute of Technical Physics at DLR. The focus will lie on the main parameters for space engineering. The second section gives an overview over solid state theory of simple metals including interactions within the materials. Since a main part of energy transport is of thermal nature one focus is thermal conductivity. In the third section an introduction into laser physics is given, basically providing information about the description and the main parameters of laser sources. The chapter ends with a detailed description of possible processes occuring in laser-matter interaction.

2.1. Applied physics: Aerospace engineering

In this section parameters important for aerospace applications and the DLR concept of laser-ablation micropropulsion (MICROLAS) are described.

2.1.1. Concept of MICROLAS propulsion

The general concept of laser-ablation micropropulsion was given by Phipps who introduced a thruster concept using ms-laser pulses [5]. Later developments used ns-laser pulses [5]. MICROLAS is a new propulsion concept of a fine tuneable and controllable thruster in the μN-regime. In principle, it should be tunable over a wide range of thrust levels by variation of the laser repetition rate which provides for a higher rate of ablated material and therefore a higher impulse transfer on the satellite. The intended structure is sketched in figure 2.1. The main and probably heaviest component is a laser source which beam propagates through a system of lenses and mirrors without any moving mechanical parts. This new concept is called inertia-free since

the only impulse change comes from the ablation process itself. This occurs when the laser beam hits the propellant plate. In experiments at DLR mainly the laser-matter interaction has been analyzed until now in the laboratory. The beam guidance is under construction, exact measureable impulse transfer facilities in vacuum were already used for measurements. First results will be discussed in chapter 4.

This work is part of a simulation project in order to understand the ablation process better and the evolution of a plasma plume expelled from the propellant plate. Modelling approaches are described in detail in section 3.1.3.

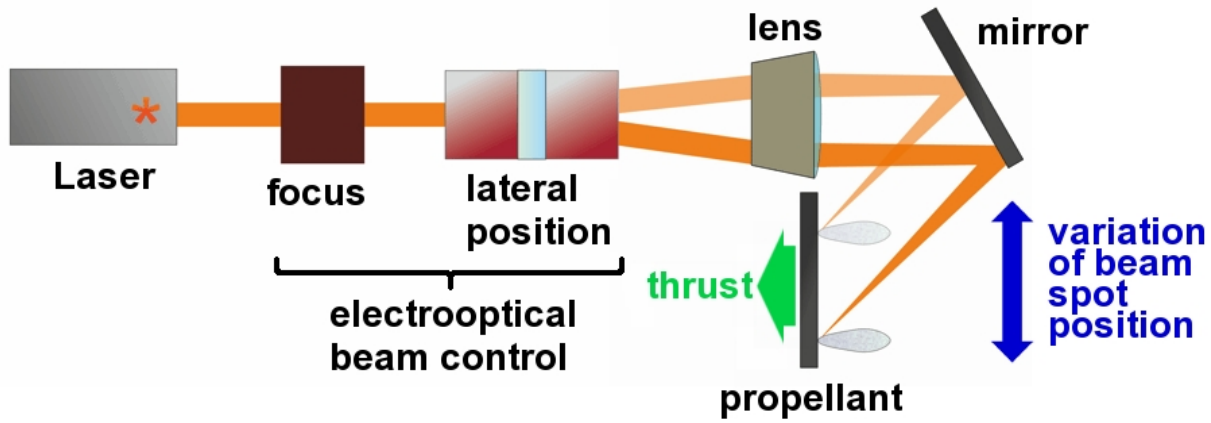

Figure 2.1.: Concept sketch of MICROLAS propulsion, adapted from [6]

Main interests in simulations on atomistic scales, on one hand, come from the ablation process itself. The question is what processes in the microscopic world have got a hard impact on macroscopic values. How are domains on the surface and within the material reorganized when a laser beam of high energy hits the target? Where does the energy go into? Does overlap of a beam spot with an already dug hole has an influence? What are the ratios of matter states and does ionization play a big role? Towards continuum, the evolution of the velocity and mass distribution in time and space is of big interest. The amount of ablated material and its potential of contamination the propulsion system itself plays a big role when looking at main mission parameters like lifetime and possible time of operation. But the relapse of the material is also important for eventual missions the MICROLAS propulsion may come into consideration for. Dirty lenses or current conducting shells may induce a variety of problems.

Other main parameters of course are the thrust one can achieve with this kind of system and how effectivity changes with material parameters of the propellant. It still is not clear which propellant to use. However, the focus in this work is on solid propellants.

2.1.2. Important parameters

Nowadays many microthruster systems for space applications are characterized by two main parameters, the so called **specific impulse** I_{sp} and **impulse coupling coefficient** C_m. The specific impulse of classic propulsion systems is defined by [7]

$$I_{sp} = \frac{F}{\dot{m}\, g} \qquad [I_{sp}] = s \tag{2.1}$$

where F is the **thrust** (force) in $Newton$ of the engine, $\dot{m}$ the mass flow rate of the propellant in kg/s and g being earth's standard acceleration on the surface measured in m/s^2. Typical values are $I_{sp,vacuum} = 455$ s of the Space Shuttle main engine, $I_{sp,vacuum} = 435$ s of a HM60 - thruster (Vulcain) of Ariane 5 and the A4 - engine with an I_{sp} of 210 s at ground level [7]. The estimated specific impulse value for the MICROLAS engine provided by one dimensional simulations was very promising, so further investigations were taken into account.

There is an alternative expression of the specific impulse,

$$I_{sp} = \frac{p}{m\, g} = \frac{\langle v \rangle}{g}, \tag{2.2}$$

whereas p is the impulse of the exhaust jet, in our case the ablated material and $\langle v \rangle$ being the mass weighted velocity of N expelled particles,

$$\langle v \rangle = \frac{\sum_{i=1}^{N} m_i\, v_i}{\sum_{i=1}^{N} m_i} \quad . \tag{2.3}$$

Since we are dealing in the simulation with point particles describing single atoms, these expressions are used mainly in the rest of this work.

The other important quantity, the impulse coupling coefficient c_m is defined by [5]

$$c_m = \frac{\Delta \mathbf{p}}{E_{laser}} \qquad [c_m] = \frac{N\ s}{J} = \frac{N}{W} \quad . \tag{2.4}$$

The ratio of the impulse change Δp to the laser pulse energy E is an important figure of merit of a propulsion system. Typical estimated values are $80 - 220\ \mu N/W$ for an ion beam induced ablation plasma thruster [8], experimental values are $800 - 1500\ \mu N/W$ for a water-confined laser-induced plasma thruster [9] and $100 - 143\ \mu N/W$ for an air-breathing lightcraft propulsion [10].
Under the assumption of a non moving sample before ablation, the formula

$$C_m = \frac{\mathbf{p}_{plume}}{E_{laser}} \tag{2.5}$$

holds, which will mainly be used in the following.

In general electrical propulsion systems are characterized by the ratio of thrust and power

$$c_m = \frac{F}{P} \quad , \tag{2.6}$$

yielding for the whole propulsion system to

$$c_{m,system} = \frac{F}{P_{total}} \tag{2.7}$$

$$= \eta_{el.-opt.} \frac{F}{P} \tag{2.8}$$

$$= \eta_{el.-opt.}\ c_m \quad . \tag{2.9}$$

Here $\eta_{el.-opt.}$ is the efficiency of the electro-optical part of the system, that for MICROLAS is the beam guidance.

2.2. Solid state theory

At first a brief introduction in atom and molecule physics is given, according to standard text books [11, 12]. What follows is a description of the solid state and the possible excitations based on [13, 14].

2.2.1. Light emission and absorption

On the atomic level the occurring processes properly can only be described by quantum physics. The atom is built out of a nucleus, that exhibits neutrons and protons, and the electronic hull. Quantum mechanically the state of the atom is described by a wave function that includes different quantum numbers. Although a quantum number can be allocated to the nucleus (nuclear spin) as well, it has less influence on effects concerning this thesis, so it is neglected. Instead, just quantum mechanics of the electronic system is of interest since it describes the interaction of light and atoms well.
An atomic wave function

$$\Psi = \Psi_{n,l,m,s} = |n, l, m, s\rangle \tag{2.10}$$

can be described by four quantum numbers, n being the principal quantum number that describes the total energy, l and m being the azimuthal and magnetic quantum number and the spin projection quantum number s. The second and third ones describe the shape of the electronic hull in energy space and refer to the common s,p,d, ... orbitals. They are filled for building the periodic system of elements by electrons, whereas the total electron number refers to the quantum number s. The periodic table's rows K,L,M, ... follow $l = 0, 1, 2, ...$, the columns follow the subshells $m = -l, -l+1, ..., 0, ..., l-1, l$, leading to one s-orbital, three p-orbitals, five d-orbitals and so on.

Since the quantum numbers are discrete, quantum states of electrons can only change in multiples of these numbers. A neutral atom which is not excited in any way is in its ground state, meaning that all electrons are filled into the orbitals regarding Pauli's principle, i.e. pairwise with antiparallel spins. If an atom is excited by an amount of energy that fits to an energy difference of the ground state to one allowed state of the atom, an electron will change its state according to this energy. These excitations can be of thermal or electromagnetic nature, i.e. interaction with light. However, not arbitrarily excitations are possible. An atom in state E_k can absorb a photon of energy $h\nu$ to be excited into a higher energetic state $E_i = E_k + h\nu$ with a probability per time of

$$W_{ki} = B_{ki}\ \omega_\nu(\nu) \qquad , \tag{2.11}$$

with the spectral energy density $\omega_\nu(\nu) = n(\nu)\,h\,\nu$. $n(\nu)$ is the number of photons in the interval $[\nu, \nu + \Delta\nu]$. Such an **absorption** is described by the Einstein coefficient B_{ki} and reduces the number of photons in the appropriate mode by one. Similarily, an induced emission of photons can be described. If an atom is already excited, it may emit a photon, induced by the radiation field, by changing its state from i to k via $E_k = E_i - h\,\nu$. The Einstein coefficient of **induced emission** is the proportional constant of the probability for this effect,

$$W_{ik} = B_{ik}\ \omega_\nu(\nu) \qquad , \tag{2.12}$$

the number of photons of the appropriate mode is increased by one. Also an atom may emit a photon spontaneously. This can happen in any direction then in contrast to the induced emission. The probability is unaffected by the outer radiation, thus

$$W_{ik} = A_{ik}^{spon} \qquad . \tag{2.13}$$

The **spontaneuous emission** is affected only by the states of the involved electrons, $\Psi_i \rightarrow \Psi_k$. All three effects schematically are given in figure 2.2. The three Einstein coefficients are related via

$$B_{ik} = \frac{g_k}{g_i}\ B_{ki} \tag{2.14}$$

$$A_{ik} = \frac{8\,\pi\,h\,\nu^3}{c^3}\ B_{ik} \qquad , \tag{2.15}$$

with the statistic weights $g = 2J + 1$ of a state with total angular momentum J. This can be derived from comparison of coefficients of probability densities in stationary equilibrium (emission rate = absorption rate), cf. [13, p.220].

Not all transitions given by the law of conservation of energy are allowed and take place. The expectation value of an electric dipole $\mathbf{p}$ in stationary case is given by

$$\langle \mathbf{p} \rangle = e \cdot \langle \mathbf{r} \rangle = e \cdot \int \Psi_i^*\ \mathbf{r}\ \Psi_i\ d\tau \qquad . \tag{2.16}$$

All quantum numbers are given as a set from index $i = (n, l, m_l, m_s)$, integration is done for the space coordinates of the electron. Since the wavefunction will change and

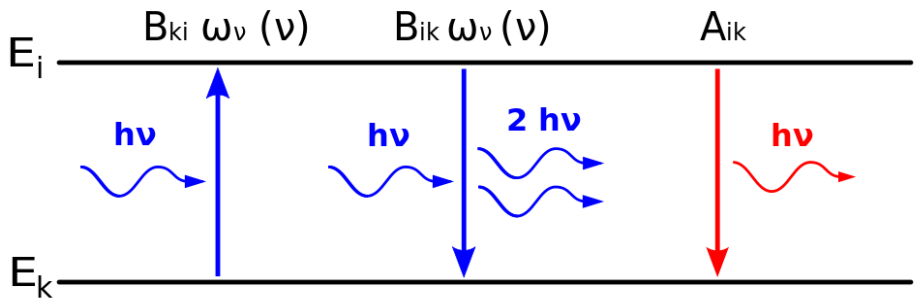

Figure 2.2.: Sketch of emission and absorption processes

describes two different states before and after photon emission, the expectation value M_{ik} of the **transition matrix element** $\mathbf{p}_{ik}$ is defined as

$$M_{ik} = e \cdot \int \Psi_i^* \, \mathbf{r} \, \Psi_k \, d\tau \qquad . \tag{2.17}$$

i and k stand for all quantum numbers of the two states. Einstein coefficients then have to take into account for the quantum mechanically allowed transitions. Equation 2.17 and a consideration of power emission of a Hertzian dipole leads to equations for the Einstein coefficients [13, p.222-224]:

$$A_{ik} = \frac{2}{3} \frac{e^2 \, \omega_{ik}^3}{\epsilon_0 \, c^3 \, \hbar} \left| \int \Psi_i^* \, \mathbf{r} \, \Psi_k \, d\tau \right|^2 \tag{2.18}$$

$$B_{ki} = \frac{2}{3} \frac{e^2 \, \pi^2}{\epsilon_0 \, \hbar} \left| \int \Psi_i^* \, \mathbf{r} \, \Psi_k \, d\tau \right|^2 \tag{2.19}$$

In molecules the spatial arrangement of the nuclei as core support structure for the electron clouds plays a big role. Whereas the electronic system can be considered separately from the nucleus when looking at atoms in most cases, this can be done for molecules just in particular cases. The bindings of nuclei in molecules directly are affected by the electronic structure and vice versa. The core support structure may have various degrees of freedom concerning rotation and vibration. The correlations between rotational, vibrational and electronic excitations lead to very complex spectra. However through mathematical instruments of representation and group theory the description and interpretation of molecular spectra by symmetry considerations is possible. Although Hamiltonians can be solved quantum mechanically for small

systems with some approximations, this is not possible for the description of the solid state. Nevertheless, mighty concepts exist given by the nature of many particle systems that describe occurring effects very properly. For details, [12] is highly recommended.

2.2.2. Crystalline solids - structures and Interactions

Chemical bondings in solids in general encompass covalent, ionic, hydrogen, van der Waals and metallic bonds. However, in this thesis the emphasis lies on the last. In metals electrons have very extent wave functions in comparison to atomic separation, e.g. the 4s wave function of Ni still has a significant amplitude at half distance to the third nearest neighbours (cf. [14, p.14]). The positive ion cores are screened and valence electrons smear out over the whole crystal. Metallic crystal structures are determined by the attempt for an optimum filling of space. The energy is distributed quasi-continuously for large atom numbers, so energy supply to electrons can be done in infinitesimally small portions, especially by an external electric field. This is a reason for the common high electrical conductivity of metals and also related to their thermal conductivity partially. The wave function overlap makes it hard to predict theoretically binding energies but simplifies the description of electrical conductivity.

The periodicity of crystals is due to the special chemical bonding, which generally results in equilibrium separations with respect to the minimization of total energy. Many identical atoms obtain a state of minimized energy when every atom is in an identical environment, which results in a three dimensional periodic arrangement, or crystalline state. Solids mixed up of different atoms arrange in periodically repeated basic units of the same inner structure. These building blocks arrange in structures that can be described by 14 basis vector systems, the so called **Bravais lattices**. Since a crystal has a periodic structure, atomic or basic cell positions can be transferred into others with symmetry operations like plane reflections, inversion and rotation. Similar to the description of molecules, group theory provides mighty tools for symmetry descriptions. For example, it can be shown that all crystals have to belong to one of 32 crystal classes (**point groups**). If the point group of a crystal is known, many statements can be made, e.g. concerning atomic wave functions.

Within a crystal consisting of N atoms, 3N stationary lattice vibrations exist with discrete frequencies Ω_K, called **phonons**, with an energy $\hbar\Omega_K$ and a quasi momentum $\hbar K$. The frequencies in general are not direct proportional to the wavevector K, but have a dispersion relation $\Omega(K)$, dependent of the spring constants of the crystal atoms. Their modes are subdivided into acoustic and optical modes. The first can be induced by mechanical vibrations, last by absorption of electromagnetic waves.

Electrons within a solid can be either localized at their atomic nuclei (inner electron shell) or delocalized. The high electrical and thermal conductivity in metals are due to delocalized electrons. Also metals are highly reflective in the optical spectrum. The simple free electron gas model treats the electrons as free within an one or a three dimensional box of side length L. The **density of states** $D(E)$, i.e. the number of occupied energy states per energy unit, is given by

$$D(E) = \frac{L^3}{4\,\pi^2}\left(\frac{2\,m}{\hbar^2}\right)\,\sqrt{E} \quad \sim\sqrt{E} \qquad . \tag{2.20}$$

in three dimensional case. All possible states to the energy E is given by

$$Z(E) = \frac{L^3}{6\,\pi^2}\left(\frac{2\,m\,E}{\hbar^2}\right)^{3/2} \tag{2.21}$$

Due to Pauli's principle, each state can only be occupied by two electrons, so at $T = 0$ K $N/2$ electrons fill all states. From equation then follows 2.21 the **Fermi energy** E_F:

$$E_F = \frac{\hbar^2}{2\,m}\,(3\,\pi^2\,N/L^3)^{2/3} \tag{2.22}$$

From a more detailed description allowing energy transfer between electrons and atoms through collisions, the well known **Fermi-Dirac distribution function** follows,

$$f(E) = \frac{1}{e^{(E-E_F)/k_B T}+1} \qquad , \tag{2.23}$$

giving the probability of finding a state of energy E filled with electrons.

Electrons travel in the periodic potential of the ion nuclei,

$$E_{pot}(\mathbf{r}) = E_{pot}(\mathbf{r}+\mathbf{R}) \qquad , \tag{2.24}$$

with **R** being the lattice translation vector. The wave functions are given by **Blochfunctions** with periodicity

$$\Psi(\mathbf{r}) = u(\mathbf{r})\ e^{-i\ \mathbf{k}\cdot\mathbf{R}} \qquad , \tag{2.25}$$

with $u(\mathbf{r}) = u(\mathbf{r}+\mathbf{R})$ being a periodic function. In the one dimensional case, the two possible solutions are given by wave functions for electrons via

$$\Psi_{\pm} = \frac{A}{\sqrt{2}}\left(e^{i\ \pi\ x/a} \pm e^{-i\ \pi\ x/a}\right) \qquad , \tag{2.26}$$

calculated from the superposition of an incoming and an outgoing wave. For the probabilities of presence equations

$$\Psi_{+}^{*}\Psi_{+} = 2\ A^2\ \cos^2\frac{\pi\ x}{a} \tag{2.27}$$

$$\Psi_{-}^{*}\Psi_{-} = 2\ A^2\ \sin^2\frac{\pi\ x}{a} \tag{2.28}$$

follow. They are given for explanation together with a periodic potential in figure 2.3. Electrons with wavefunction Ψ_{+} mainly are located next to ions and therefore have a higher energy as electrons of type Ψ_{-}, due to their higher coulomb potential. For $k = \pm\ \pi/a$ (edges of first Brillouin zone) the electronic energy splits up into

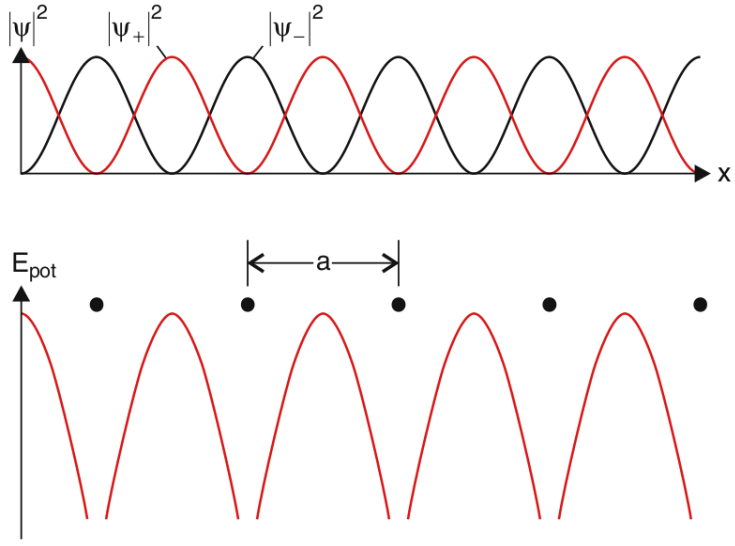

Figure 2.3.: Solution wavefunctions of electrons in a one dimensional crystal with periodic potential E_{pot}, adapted from [13]

two values. This effect is called **band splitting** or building of an energy gap. Due to the finite size of a crystal lattice external boundary conditions exist, resulting in discrete energy levels, but also for small crystals they smear out and can be treated as quasi-continuous. These energy bands can be filled at maximum with 2N electrons. The three categories in electricity, i.e. insulator, semiconductor and conductor follow from the filling of the bands. The highest completely filled band is called **valence band**, whereas the next higher band is called **conductance band**. If the Fermi energy is between the energies of the two bands, the probability of an electron can not be rised significantly by an outer voltage to surpass the energy gap. The material is an insulator then, because the valence band completely filled with electrons allows no charge transport. If the Fermi level lies within the energy of a band, it is partially filled, and electrons may travel if an outer voltage is applied. Good or bad conductors are given by the width of their band gaps and, depending on the width, are declared as semiconductors. Within real solids the band structure is much more complicated than indicated here due to several correlations between involved particles and quasi particles. However, this is not discussed in detail.

The transport of heat in solids in general is done by phonons and free electrons. The latter dominate the heat conduction within metals. As a wrap-up, in the following table all important particles and interaction from the atomic to the macroscopic world is given.

Table 2.1.: From the atomic to the macroscopic world

<table>
<tr><th colspan="2">atoms</th><th>molecules</th><th>solid state</th><th>(quasi) particles</th><th>macroscopic</th></tr>
<tr><td rowspan="2">nucleus</td><td rowspan="2">nuclear spin</td><td>vibrational states</td><td>periodic order</td><td rowspan="2">phonons</td><td>crystal structure
phase transitions</td></tr>
<tr><td>rotational states</td><td>lattice dynamics</td><td>heat conductivity</td></tr>
<tr><td rowspan="3">electronic hull</td><td rowspan="2">electronic shell and subshell</td><td rowspan="3">electronic states</td><td>band model</td><td>electrons</td><td>electric conductivity</td></tr>
<tr><td>electromagnetic waves</td><td>photons</td><td>optics</td></tr>
<tr><td>electron spin</td><td>magnetic order</td><td>magnons</td><td>magnetism, superconductivity</td></tr>
</table>

2.3. Laser physics

2.3.1. Light sources

In principle two sorts of light sources can be distinguished according to their spectra. **Continuous light sources** as the sun or classical light bulbs show a spectrum that includes a variety of wavelengths that merge into each other continuously, whereas **discrete light sources** show (more or less) exactly defined wavelengths in their emission (or absorption) spectra. With invention of the **laser** a discrete light source was accessible with additional unique properties like monocromaticity and coherence. Monocromaticity means that the spectrum includes just one discrete wavelength (a Lorentz profile), coherence refers to a constant phase relation of two electromagnetic waves.

The acronym LASER stands for "Light amplification by stimulated emission of radiation". The first devices amplifying electromagnetic radiation by stimulated emission operated in the microwave regime [15] and were therefore called **masers**. After Schawlow and Tones showed that infrared and visible light also can be amplified [16], in 1960 Maiman introduced the first solid state laser with ruby as a gain medium [17]. Developments of gas lasers as CO_2-, He-Ne- or Excimer-lasers followed, in the 1970's dye lasers occured being tunable over several wavelengths [18].

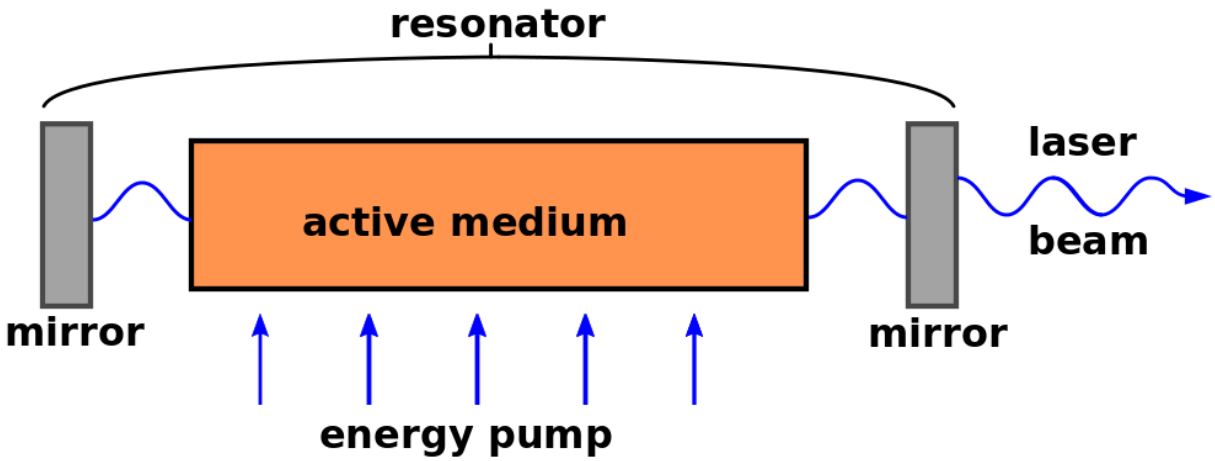

Figure 2.4.: Basic sketch of a laser

Lasers are built of three main parts that include several mentioned aspects (compare figure 2.4):

Active medium Selective energy supply to one or multiple niveaus results in a population inversion that differs from thermal equilibrium. Higher niveaus are more populated than lower niveaus.

Energy pump Creates occupation inversion, e.g. flashbulbs, gas discharges or lasers.

Optical resonator Stores fluorescence from the active medium in a few radiation field modes. The selected modes have high photon numbers so the probability of stimulated emission overcomes spontaneous emission. Also the resonator leads the radiation back into the medium for multiple passages. In figure 2.4 this is realized by two mirrors, the left one having a reflectivity of ≈ 1, the right one having a lower reflectivity to let the laser beam propagate out of the system.

If amplification surpasses losses the laser is active. Absorption, spontaneous and stimulated emission of photons by atoms have been described in section 2.2.1 already. Since spontaneous emission will always lead to a less occupation of excitation states of atoms, a material providing a two-niveau system is not usable for lasers. Instead **multiple niveau systems** are in use.

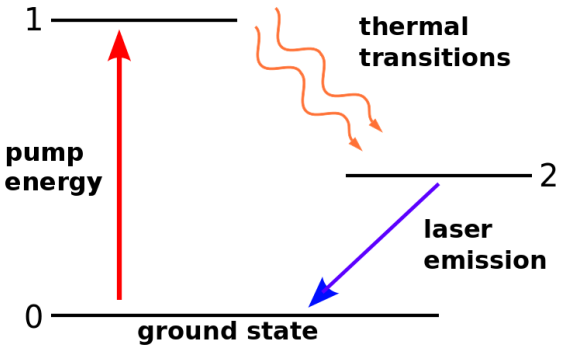

Figure 2.5.: Sketch term diagram of ruby laser

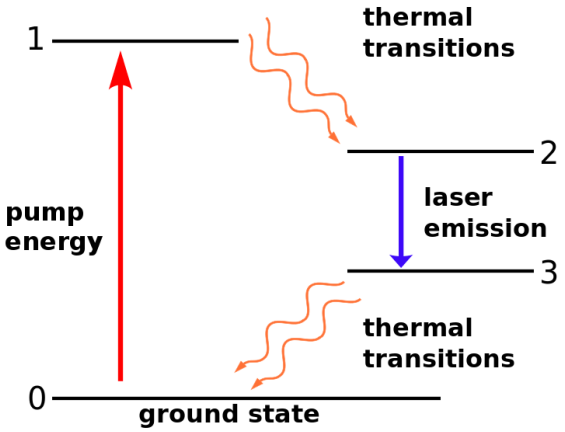

Figure 2.6.: Sketch term diagram of a 4-niveau laser

An example is given by the term diagram of the ruby laser, figure 2.5 (left). Pumping brings in energy to excite the system from ground state (0) into a higher energetic

state (1). The transition of the system from state (1) to (2) happens very fast compared to the transition (1) to (0), written in terms of population numbers N_i

$$N_1 \approx 0 \tag{2.29}$$

$$N = N_0 + N_1 + N_2 \approx N_0 + N_2 \quad , \tag{2.30}$$

with N being the total number of occupied states. The energy transfer is due to thermal transition or spontaneous emission. Transition (2) to (0) occurs by stimulated emission of laser light by a photon of the same wavelength (or spontaneous emission). The rate equations follow

$$\frac{d\,N_0}{dt} = -B\;I\;N_0 + A\;N_2 \tag{2.31}$$

$$\frac{d\,N_2}{dt} = B\;I\;N_0 - A\;N_2 = -\frac{d\,N_0}{dt}, \tag{2.32}$$

where A is the Einstein coefficient of spontaneous emission, B of absorption and I the lights intensity within the resonator. After subtraction, introduction of **inversion** $\Delta N = N_2 - N_0$ and using equation (2.30)

$$\frac{d\,\Delta N}{dt} = \frac{d(N_2 - N_0)}{dt} = 2\;B\;I\;N_0 - 2\;A\;N_2 \tag{2.33}$$

$$= B\;I\;N - B\;I\;\Delta N - A\;N - A\;\Delta N \tag{2.34}$$

is obtained. Operation in equilibrium is of interest, so in stationary case $\frac{d\Delta N}{dt} = 0$ equation

$$\Delta N_s = N\,\frac{I/I_s - 1}{I/I_s + 1} \tag{2.35}$$

holds with $I_s = A/B$ being the saturation intensity. If $I > I_s$, the inversion ΔN is positive, so an occupation inversion is possible. However, a minimum of half of the atoms in the highest state is necessary to enable laser light emission. When examining a **4-niveau system** as follows, a fourth niveau N_3 is introduced as in figure 2.6. As

conditions transitions (3) to (2) and (1) to (0) shall happen fast compared to (2) to (1). Then the equations

$$N = N_0 + N_1 + N_2 + N_3 \approx N_0 + N_2 \tag{2.36}$$

$$\Delta N = N_2 - N_1 \approx N_2 \tag{2.37}$$

hold. The derivation is similar to the 3-niveau system, it follows

$$\Delta N = N \frac{I/I_s}{I/I_s + 1} \quad . \tag{2.38}$$

In this case, for every intensity I the inversion is $\Delta N > 0$, making such a system a perfect laser medium.

2.3.2. Laser parameters

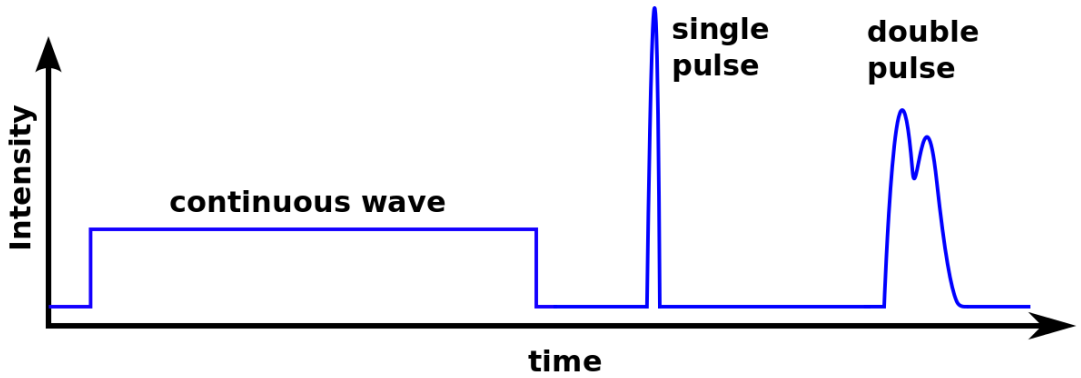

Figure 2.7.: Comparison of different lasers by intensity shape

Lasers are subdivided into **pulsed** and **CW sources**, where CW denotes for continuous wave, i.e. the light intensity can be kept constant over a longer time (up to days). Their **intensity shapes** are sketched in figure 2.7. In this thesis, just pulsed lasers of Gaussian shape in time and of TEM_{00} mode are of interest. They can be described by a few parameters which are explained in the following. The intensity of TEM_{00} mode of a laser pulse with a Gaussian temporal shape, centered at $\mathbf{x} = \mathbf{0}$ and $t = 0$ (cf. fig 2.9) is described in cartesian coordinates via

$$I(x, y, z, t) = I_0 \left(\frac{\omega_0}{\omega(z)}\right)^2 e^{-\frac{(x^2+y^2)}{\omega(z)^2}} e^{-\frac{1}{2}\frac{t^2}{\sigma_t^2}} \quad , \tag{2.39}$$

with

$$\omega(z) = \frac{\omega_0}{2}\sqrt{1+\left(\frac{z}{z_0}\right)} \tag{2.40}$$

being the transversal profile of the laser, and

$$z_0 = \frac{\pi\,\omega_0^2}{\lambda} \tag{2.41}$$

being the Rayleigh length. In this work, a Gaussian beam is assumed with perfect focus, so $\omega(z) = \omega(z_0) = \omega_0$ is always a constant (compare figure 2.9).

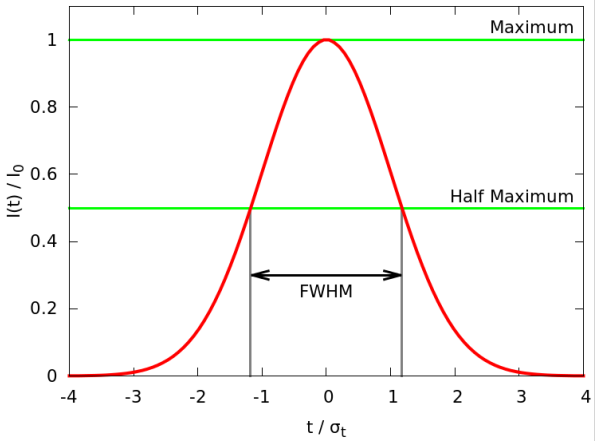

Figure 2.8.: An example of FWHM for Gaussian shapes

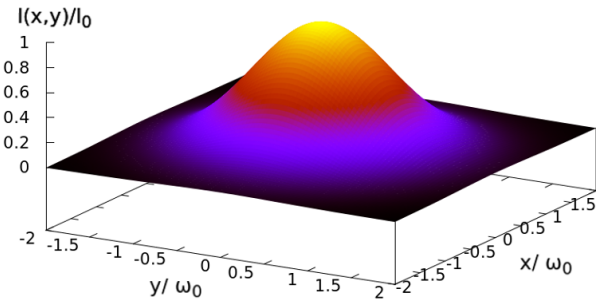

Figure 2.9.: Example plot of a TEM_{00}-mode

In experimental work lasers are usually classified by their **pulse duration** as a temporal figure of merit. This value itself has different definitions, mainly the "full width half maximum" time $t_{pulse} = t_{FWHM}$ is used in this work. Its simplicity makes it usable for the description of many pulse shapes and functions. It is just given by the difference of two points of the time, where the intensity has the half value of its maximum. For clarification, compare figure 2.8. For a Gaussian beam, t_{FWHM} is given by

$$t_{FWHM} = 2\sqrt{2\ln 2}\,\sigma_t \approx 2.35482\,\sigma_t \quad . \tag{2.42}$$

The **fluence** Φ is another classification value, i.e. the energy area density of a laser pulse:

$$\Phi = \frac{E}{A} \qquad [\Phi] = \frac{J}{m^2} \tag{2.43}$$

Also a **power** P is usually given and the electro-optical **efficiency** η of a laser is defined via

$$\eta_{el.-opt.} = \frac{P_{laser}}{P_{supply}} \quad , \tag{2.44}$$

with P_{supply} being the power of the power supply unit and P_{laser} being the power provided by the laser beam. These parameters are of high interest for the configuration of laser experiments.

2.3.3. Laser-Matter Interaction

Light energy is coupled into matter by different processes, according to the energy of the incident photons. Most probable excitations are single photon excitations of atoms or molecules of a material, although multi-photon processes also often are involved or even dominant. If the photon energy is high enough, chemical bonds directly can be broken. However, many material changes of mechanical and optical nature are due to thermal excitations within the material. Temperature rises may induce stresses and defects, resulting in material changes.

If short pulsed lasers induce ablation phenomena on material surfaces, the electrons are the most important species involved. They are excited and transport heat into the sample within the electronic system which over time is dissipated into the ionic lattice, leading to bond breaking if high enough. Theoretically this is covered by the **two temperature model**, described in detail in section 3.1.3. The governing equations can only be solved numerically.

3. Computational concepts

After an introduction to the main tasks related to the concept of MICROLAS propulsion, physical theories of all important fields for this work were introduced. The following chapter has its focus on the simulations of the previous topics. First a general overview over Molecular Dynamics simulation is given, followed by an introduction to the simulation of the solid state and its interaction with the laser beam. Finally, alternative models and software packages briefly are discussed.

3.1. Molecular Dynamics and the IMD code

In **Molecular Dynamics** (MD) simulations point particles interact with each other under the influence of inter particle potentials $V(r)$. The particles have well defined spatial coordinates and vectorial velocities. Interaction potentials themselves are the backbone of any MD simulation - if they do not describe the material well and take most physical interactions into account, no connection to the real world can be made. The potentials that were used in this thesis and included interactions are stated in section 3.1.1.

Under the assumption that the interactions are described well by potentials $V(r)$, in MD Newton's equations of motion are solved by programs called **integrators**. In IMD a **verlet type integrator** is used. Each simulation step $t \rightarrow t + \Delta t$ the forces are calculated out of the interaction potentials by the negative gradient

$$\mathbf{F} = -\nabla\, V(\mathbf{r}) = -\nabla\, V(r) \quad , \tag{3.1}$$

whereas the second part comes from the assumption that the interactions just exhibit a proportionality to the distance. This is appropriate for the potentials used in this thesis, but in general solid state potentials that include an angle dependency or

a favoured state of a material at special phase transitions of crystals are in use, to mention just two examples.

To integrate the equations of motion, the impact of the forces on the motion of the particles is considered by a **leapfrog integrator** scheme: [4]

$$\mathbf{r}(t + \Delta t) = \mathbf{r}(t) + \frac{\Delta t}{m}\, \mathbf{p}(t + \frac{1}{2}\Delta t) \tag{3.2}$$

$$\mathbf{p}(t + \frac{1}{2}\Delta t) = \mathbf{p}(t - \frac{1}{2}\Delta t) + \mathbf{F} \cdot \Delta t \tag{3.3}$$

Until now, the total energy of the simulated system is constant (**NVE**-Ensemble). At the beginning of a simulation run, potential and kinetic energies are exchanged until the system is in an equilibrium state. So even if a crystal structure is fine tuned at the beginning, a velocity distribution once well defined at the beginning is newly distributed by the interaction of the particles. If one defines a Maxwellian velocity distribution to get a desired temperature on the system, after the first simulation steps the kinetic energy partially changes into potential energy, thus the temperature varies from the initial one. For getting a desired temperature into a system, an outer heat bath is coupled to it. This is an integration in the **NVT**-Ensemble, and there exist different forms of methods coupling in the external energy. They are called thermostats and differ in the way they couple the energy into the system. Calculation time consuming ones often have special properties important for different purposes, e.g. they conserve properties important for correct thermodynamic statistics. For details, see [19]. In IMD, the standard thermostat is of Nosé-Hoover type.

3.1.1. Potentials

Metal atomic interactions of the simple metals aluminium and gold are modelled using **EAM**-potentials, short for **E**mbedded **A**tom **M**ethod-potentials. In general these are multi-body potentials that take into account for interactions of neighbouring atoms. The description of the interatomic interaction potential V_i of an atom with index i is given by three functions ϕ, F and ρ

$$V_i = \frac{1}{2} \sum_{ij, i \neq j} \phi(r_{ij}) + F\left(\sum_j \rho(r_{ij}) \right) \quad , \tag{3.4}$$

with $\phi(r_{ij})$ being the core-core interaction of two atom cores with indices i and j, F being the embedding function which describes the interaction of the electron hulls between one atom i with all neighbour atoms j, whereas the influence of electron densities is given by $\rho(r_{ij})$, the atomic density function. All three functions are individual for each metal. An intiutively accessible view on $\rho(r_{ij})$ is the electron density of the atoms, although in general this is an empirical function that comes from the interplay of all orbitals and correlations between them, distributed over all atoms within a specific range. A sample plot for aluminium is given in figure 3.1. The local electron density ρ nearly reproduces the well known lattice constant of 4.0531 Å, since at $r \approx 5$ Å it shows a maximum. Other effects are included here, so the two values are not the same. Also from the attraction potential F it can be seen that the strongest attracting force on an aluminium atom occurs at the surface to hold it back: In fcc structures at an even surface an atom has 10 neighbours so the sum over all densities gives ≈ 1, where the potential has a minimum. ϕ shows an classical repulsive potential of $1/r$ -type.

There are various methods to find EAM potentials. In principal, all use different atomic configurations being representative for metals like clusters, surfaces, defects in crystals and atoms in liquid and gas phase, respectively. The potentials originally were fitted empirically, so Daw and Baskes showed the three functions Φ, F and ρ directly correspond to measurable quantities of crystals like lattice constants, elastic constants, sublimation energy and vacancy-formation energy [21]. Also the functions can be directly calculated out of quantum mechanical systems simulated by first principle calculations, e.g. by DFT or tight binding formalism. Ercolessi and Adams for example introduced a method to fit potentials from forces out of many atomic configurations, called force-matching method [20]. Nowadays often hybrid methods are used, including both ab-inito simulational and experimental data. One fitting tool called **potfit** was developed at ITAP [22].

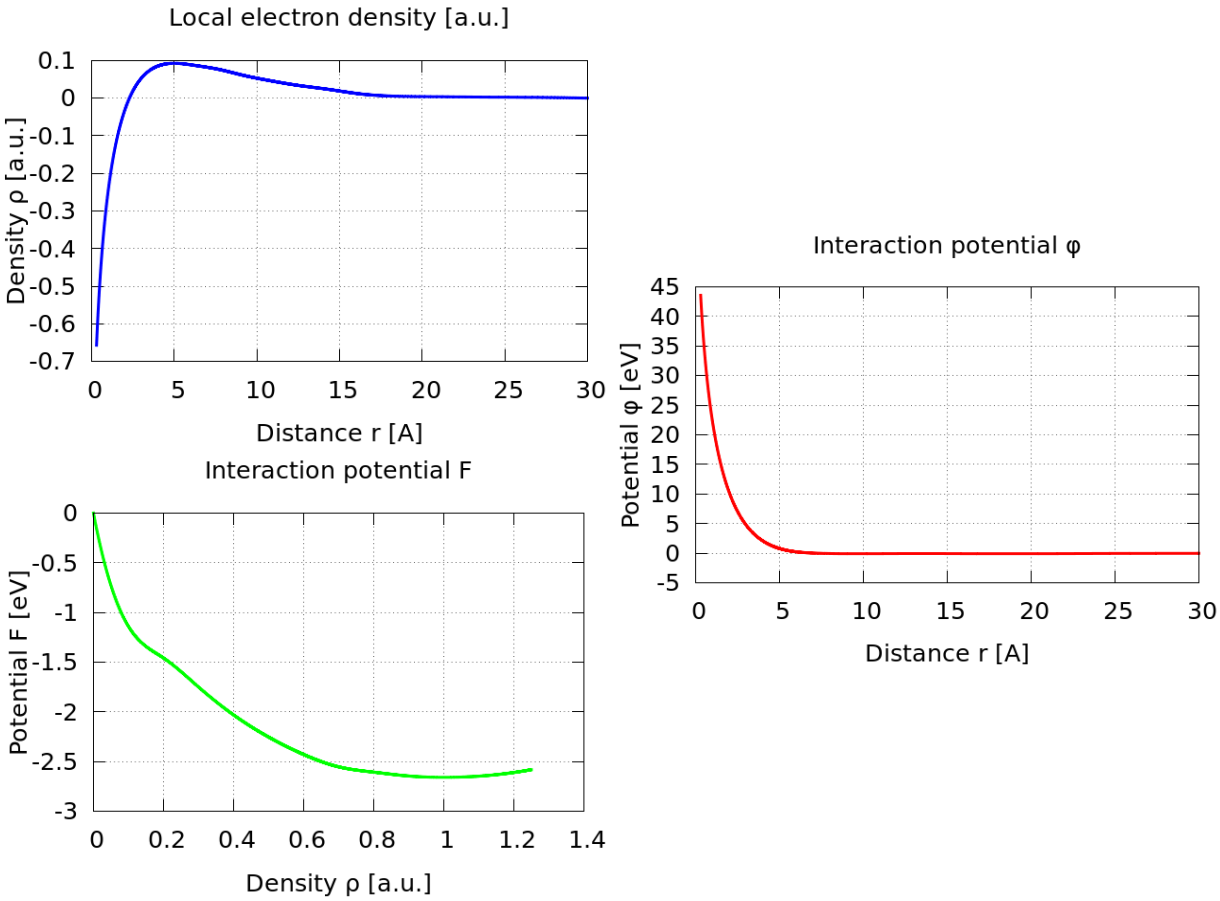

Figure 3.1.: Example plots of functions ρ, F and ϕ for aluminium [20]

3.1.2. Laser-matter interaction - the rescaling model

In general laser beams are treated in the software IMD as energy sources that are described by a temporally and spatially varying energy density within the material. For more computational details see [4] and [23], the following equations are stated mainly according to these authors.

There are two main models implemented in IMD to couple in laser energy. The rescaling model, refered to as **RES**-model in the rest of this work, rescales the velocities of atoms according to the distribution of the laser beam in space and time. It is done by coupling the laser energy to the kinetic energy of the atoms, following

$$E_{kin,j}(t+\Delta t) = E_{kin,j}(t) + \frac{\Delta t}{\rho}\, S(\mathbf{r},t) \qquad . \tag{3.5}$$

j is an atom index, ρ stands for the density, i.e. the volume per atom and S being the laser source term. In case of modelling the influence of band electrons on heat flow within the sample, the **TTM**-model is used. It is described in section 3.1.3 in detail.

A general laser source term used here exhibits the temporal shape of a Gaussian pulse:

$$S(x,y,z,t) = S_0 \;\; e^{-\frac{1}{2}\frac{(t-t_0)^2}{\sigma_t^2}} \;\; I(y,z)\; e^{-\mu x} \qquad . \tag{3.6}$$

Here σ_t is the time at which $S(\mathbf{r},t)$ decreased to a value of $1/\sqrt{e}\; S_0$, t_0 is the time of the peak maximum. In x-direction the in brought laser energy is decaying via the **Lambert-Beer's law** with μ being the inverse absorption length, $[\mu] = m^{-1}$, at which the intensity in x-direction decreased to $1/e\; S_0$. Two special cases of spacial resolution $I(\mathbf{r})$ are used in this work: One is the TEM_{00} Mode,

$$S(x,y,z,t) = S_{3D} \;\; e^{-\frac{1}{2}\frac{t^2}{\sigma_t^2}} \; e^{-\frac{y^2+z^2}{\omega_0^2}} \; e^{-\mu x} \qquad , \tag{3.7}$$

whereas S_{3D} has the dimensions of an power density $[S_{3D}] = \frac{[P]}{[x]^3} = \frac{W}{m^3}$ and ω_0 being the characteristic length. This often in literature is refered to as the beam waist or spot size, since within a circle of area $2\pi \cdot 3\omega_0$ most laser energy is absorbed within the material (about 99.73 %). Another form is given by $I(y,z) = 1$, describing homogenous irradiation. S_0 then is an one dimensional power density with $[S_{1D}] = \frac{W}{m}$, the spatial evolution is just covered by the Lambert-Beer's law then.

The parameters in simulations can be connected directly with common laser parameters used in experiments. By integration over time and space the **total laser energy** is provided via

$$E = \frac{(2\pi)^{3/2}\; S_{3D}\; \sigma_t\; \omega_0^2}{(1-R)\; \mu} \qquad . \tag{3.8}$$

By integration over time and just the x-coordinate the **fluence**

$$\Phi = \frac{\sqrt{2\pi}\; S_{1D}\; \sigma_t}{(1-R)\; \mu} \tag{3.9}$$

can be derived. The reflectivity R is a unitless percentual constant that is fixed and is introduced during integration via

$$E \cdot (1 - R) = \int S(\mathbf{r}, t) \qquad . \tag{3.10}$$

Since the usual used quantity in IMD to define the brought in energy is the fluence parameter σ_e, the reflectivity R is used as conversion parameter via

$$\Phi = \frac{\sigma_e}{(1 - R)} \qquad . \tag{3.11}$$

3.1.3. Two-Temperature model

Metallic samples being in thermal equilibrium can be described simply by the interactions already mentioned. The atoms exchange energy via the interaction potentials, while slow heating of a sample can be done by rescaling of the kinetic energies, i.e. the velocities.
When energy is coupled in by photons, the electrons react on incident radiation by gaining energy. The energy transport over the sample is not any longer just driven by collisions of atoms but by quantum mechanical effects as described in section 2.2. Since it is not directly possible in MD simulations to consider quantum effects yet, a macroscopic model was implemented to describe the heat transport within metallic samples properly. All equations, as in the section before, follow [4] and [23]. The **two temperature model** (TTM) describes the evolution of heat with three measurable main parameters in a set of nonlinear differential equations [4]:

$$C_e(T_e)\frac{\partial T_e}{\partial t} = \nabla[K_e \nabla T_e] - G(T_e - T_l) \tag{3.12}$$

$$C_l(T_l)\frac{\partial T_l}{\partial t} = \nabla[K_l \nabla T_l] \; + G(T_e - T_l) \tag{3.13}$$

The indices e and i here stand for parameters concerning *electrons* and *ions*. The heat transfer from the electron subsystem to the lattice is described by the term $(T_e - T_l)$, with G being the electron-phonon coupling constant. $C_{e,l}$ are heat capacities of the

subsystems, $K_{e,l}$ are heat conductivites. The laser source term can be coupled to the heat equations via the electronic system via a laser power density term $S(\mathbf{r}, t)$:

$$C_e(T_e)\frac{\partial T_e}{\partial t} = \nabla[K_e \nabla T_e] - G(T_e - T_l) + S(\mathbf{r}, t) \tag{3.14}$$

$$C_i(T_l)\frac{\partial T_l}{\partial t} = \nabla[K_i \nabla T_l] \ + G(T_e - T_l) \tag{3.15}$$

Its behaviour in time and space is described in detail in section 3.1.2. The phenomenological TTM equations describe heat transport in continuum, so usually they are solved by **finite difference schemes** (FD). Since we are on atomistic level, just the electronic heat transport is described in continuum as in equation (3.12). The ionic movement is of course influenced by the behaviour of the electrons, but their positions directly refer to atomic coordinates in the MD simulation. A hybrid simulation model was implemented in IMD in the following way, according to [24]:

$$C_e(T_e)\frac{\partial T_e}{\partial t} = \nabla[K_e \nabla T_e] - G(T_e - T_l) + S(\mathbf{r}, t) \qquad \text{FD} \tag{3.16}$$

$$m_i \frac{\partial^2 \mathbf{r}_i}{\partial t^2} = \mathbf{F}_i + \xi \, m_i \, \boldsymbol{v}_i^T \qquad \text{MD} \tag{3.17}$$

$$\xi = \frac{\frac{1}{n}\sum_{k=1}^{n} G \, V_N \, (T_{e,k} - T_l)}{\sum_j \, m_j \, (v_j^T)^2} \qquad \texttt{coupling} \tag{3.18}$$

m_i, $\mathbf{r}_i$ and $\mathbf{F}_i$ correspond to the MD system, the index i stands for an atom, the forces $\mathbf{F}_i$ come from the inter atomic interactions. The ions and electrons are calculated within two different systems, one belonging to MD space, the other to FD space, in which the electron heat transport is calculated. Here, the so called thermal velocity $v_i^T = v_i - v_{com}$ is introduced, where v_{com} is the center of mass velocity of atoms in a FD cell. The two systems are coupled via ξ, both systems have different calculation time steps, the FD system is solved more often, n gives the ratio of both time steps. Within one MD step n FD steps are calculated. k runs over all FD calculations within one MD step, j is a summation over all atoms within one FD cell.
The discretization time step of the electron system has to fulfil a stability criterion, so that the transferred energy between the two systems does not give rise to an accumu-

lation that lets the MD system unphysically burst (or "freeze" because of too much energy extracted) . It holds

$$n \geqslant \frac{2\,\Delta t\,K_e}{x_{FD}\,\min(C_e))} \quad , \tag{3.19}$$

with Δt being a MD timestep, x_{FD} the minimum thickness of an FD cell and $\min(C_e)$ the minimal electron heat capacity occurring in the simulation.

The implemented interactions in IMD already have shown often that the simulation results show good agreements with experimental results in the fs-laser pulse regime [25, 4]. However, there are frontiers. First of all, a particle based algorithm that directly takes quantum effects into account would perfectly describe the atomistic world. All described effects occuring on this level are excluded until now. Instead, a continuum model for heat transfer describes occuring processes, all material parameters needed for this model are experimentally accessible. Most parameters are defined constant at present, although in principle all at least are temperature dependent:

electron-phonon coupling parameter	$G(T) := G$
heat capacity	$C(T) := \gamma \cdot T$
thermal conductivity	$K(T) := K$
reflectivity	$R(T, \lambda, P) := R$

First principle calculations show that even the behaviour of simple metals differs dramatically from assumptions of this kind in non-equilibrium conditions [26]. Deviations occur for aluminium, copper and gold in heat conductivity C and the electron-phonon coupling factor G. For C, a simple relation is already implemented, assuming a linear behaviour. Here deviations lie in the range of decades, so the linear approximation covers this partially although the shape is not completely right. K and G deviate for aluminum at the same magnitude as the values themselves, so the constant approximation should represent measured effects quite well. Reflectivity, however, in general is dependent of at least three physical values being temperature T, wavelength λ and polarization P. Even these have correlations among each other, depending on the material. As calculations and measurements for aluminium at $\lambda = 0.69\ \mu m$ show, reflectivity drops over a wide range of non-equilibrium temperature increase in the range of $R \in [0.57, 0.85]$ in a temperature range from 0 K to 920 K, the occuring mechanisms still are not completely understood [27].

3.2. Hydrodynamic model - Virtual Laser Lab

At the Institute of Technical Physics, DLR Stuttgart, initial estimation parameters for MICROLAS propulsion are obtained by using the **Virtual Laser Lab** (VLL). VLL is an online tool for one-dimensional calculations of laser matter interactions, e.g. the behaviour of thin metal foils has been simulated properly [28]. The following introduction of this hydrodynamic model follows the same source.

3.2.1. Light absorption and reflectivity in VLL

Light absorption and reflection in this model follow classical electrodynamics, while non-equilibrium states of matter are taken into account by a two-temperature approximation. The permittivity $\epsilon(z)$ of a material is defined piecewise constant in z-direction and introduced in the Maxwellian equations (for s-polarised light) via

$$\frac{\partial^2 E_y}{\partial z^2} + k_L^2 \left[\epsilon(z) - \sin^2\theta\right] E_y = 0 \tag{3.20}$$

$$\frac{\partial^2 B_y}{\partial z^2} + k_L^2 \left[\epsilon(z) - \sin^2\theta\right] B_y - \frac{\partial \ln \epsilon(z)}{\partial z}\frac{\partial B_y}{\partial z} = 0 \quad , \tag{3.21}$$

with E_y and B_y being the electric and magnetic fields in y-direction perpendicular to the laser propagation in z-direction. k_L is the laser frequency, c the speed of light and θ the incidence angle. These equations have exact solutions of type

$$F_m(z) = f_m^{(+)}\, e^{i\, k_m (z - z_m)} + f_m^{(-)}\, e^{-i\, k_m (z - z_m)} \quad . \tag{3.22}$$

Here the arbitrary zone in z-direction is discretized in steps $z_m \leqslant z \leqslant z_{m+1}$, $m = 0, ..., N-1$ and $k_m = k_L \sqrt{\epsilon_m - \sin^2\theta}$. This can be solved iteratively after some derivations assuming continuity and first derivative jumps. The laser absorption term can be written as

$$Q_m = \frac{I(t)\; k_L\; \mathrm{Im}(\epsilon_m)}{z_{m+1} - z_m} \int_{z_m}^{z_{m+1}} |\mathbf{E}(z)|^2 \; dz \quad , \tag{3.23}$$

with

$$|\mathbf{E}(z)|^2 = \begin{cases} |E_y|^2 & \text{for S-polarisation} \\ |E_x|^2 + |E_z|^2 & \text{for P-polarisation} \end{cases} \quad . \tag{3.24}$$

The reflectivity R and transmission T are well known then by $R = \left| f_o^{(-)} / f_o^{(+)} \right|^2$ and $T = \left| f_N^{(+)} / f_o^{(+)} \right|^2$.
The optical properties are described by a two state model. It includes a **metal regime**, where the temperature is below Fermi level T_F and the permittivity is given by the sum of band-to-band contributions and an intraband Drude term,

$$\epsilon_{met}(\omega_L, \rho, T_i, T_e) = \epsilon_{bb} + 1 - \frac{n_e}{n_{cr}\,(1 + i\,\nu_{eff}/\omega_L)} \quad . \tag{3.25}$$

The **plasma regime** describes hot states with $T_e \gg T_F$ via

$$\epsilon_{pl}(\omega_L, \rho, T_e) = 1 - \frac{n_e}{n_{cr}\left[K_1(\xi) - i\,\frac{\nu_{pl}}{\omega_L}\,K_2(\xi)\right]} \quad . \tag{3.26}$$

The functions K_1 and K_2 are optimized functionals for the plasma description, cf. [29]. ν_{pl} is the plasma frequency, ν_{eff} an effective frequency of collisions, n_e the concentration of electrons and n_{cr} a critical concentration where transition between the regimes takes place. The two states are interpolated between through

$$\epsilon = \epsilon_{pl} + (\epsilon_{met} - \epsilon_{pl}) e^{-A_4\ T_e/T_F} \quad . \tag{3.27}$$

Several constants, e.g. A_4, are adjusted to meet room temperature conditions for different metals and include experimental data of self-reflectivitiy and pump-probe measurements.

3.2.2. Hydrodynamic TTM simulation in VLL

The substantial reaction to the laser irradiation is covered by a hydrodynamic model of a single fluid two temperature model. Equations

$$\frac{\partial(1/\rho)}{\partial t} - \frac{\partial u}{\partial m} = 0 \tag{3.28}$$

$$\frac{\partial u}{\partial t} + \frac{\partial(P_i + P_e)}{\partial m} = 0 \tag{3.29}$$

$$\frac{\partial}{\partial m}\left(\rho\,\kappa_e \frac{\partial T_e}{\partial m}\right) - \frac{\partial S}{\partial m} + \frac{Q_L}{\rho} - \gamma_{ei}\frac{T_e - T_i}{\rho} = \frac{\partial e_e}{\partial t} + P_i\,\frac{\partial u}{\partial m} \tag{3.30}$$

$$\gamma_{ei}\frac{T_e - T_i}{\rho} = \frac{\partial e_i}{\partial t} + \,P_i\,\frac{\partial u}{\partial m} \tag{3.31}$$

include conservation of mass, momentum and energy of electrons and ionic subsystem (indices e and i). P denotes pressure, m mass, u velocity and e specific energy. The energy is exchanged via coupling described by the coefficient γ_{ei}. κ_e is the thermal conductivity coefficient of the electrons, so equations 3.30 and 3.31 are comparable to the IMD two temperature model, with Q_L being the laser source term described in equation 3.23. However additional terms exist due to the modelling in continuum and other modifications, so pressure is calculated in atomistic modelling by statistics of the particles movements and positions, for example. The value S also includes an extension not implemented in IMD - the radiation of the sample itself. $S = \int_\omega S_\omega \, d\omega$ is the integral of the spectrum density of radiation flux, whereas S_ω is calculated from a radiation flux model in a diffusion approximation. For further details, compare [28].

As can be seen this continuum model is quite complex and covers many physical effects, partially on a phenomenological basis, most based on detailed microscopic models. However, calculations are just possible in one dimension, which is a disadvantage since the laser pulses have spatial distribution which differs significantly from a simple step function ("top hat"). Additionally, volume effects may influence crater formation. Nevertheless, this is a good starting point for estimations and can be compared more or less directly to quasi-one-dimensional IMD simulations. In principal, it is possible to simulate all sorts of metals with both algorithms, unfortunately on the website of VLL only few materials can be selected up to now, i.e. aluminium, gold

and water [30]. IMD is open source software and may use different materials, just the potentials have to be specified. A variety of potential sets is available.

3.3. PICLas - Simulation of Plume

In parallel to the investigations concerning the ablation itself, the validation of the **PICLas** code of the Institute of Space Systems (IRS), University of Stuttgart, for plume simulation after ablation was performed in [31]. The code is introduced briefly in this section.

It is divided into the PIC part - short for Particle In Cell - and a DSMC part - short for Direct Simulation Monte Carlo. Basis is the Boltzmann equation

$$\frac{\partial f_i}{\partial t} + \underbrace{\mathbf{c}_i \nabla_x f_i}_{\substack{\text{spatial} \\ \text{inhomogenity} \\ \text{diffusion}}} + \underbrace{\frac{\mathbf{F}_i}{m} \nabla_c f_i}_{\substack{\text{external} \\ \text{forces} \\ \text{PIC}}} = \underbrace{\left.\frac{\partial f_i}{\partial t}\right|_{collision}}_{\substack{\text{particle} \\ \text{collisions} \\ \text{DSMC}}} , \tag{3.32}$$

that describes the temporal evolution of the velocity distribution function f_i of species i under the influence of external forces, here provided by electromagnetic fields and particle collisions.
As common in Monte Carlo schemes, random numbers are drawn. If a criterion is fulfilled according to the energy given by temperature, collisions happen or not if two particles enter the same simulation cell. Ion recombination and Coulomb collisions will be taken into account in future developments.
The PIC code is a self-consistent calculation of electrical and magnetic field out of the Maxwell equations. In each step from the particles within a cell the fields are calculated, so flux $\mathbf{j}$ and density ρ are interpolated onto the grid. Then the grid fields are used to calculate the forces that act on the particles. Afterwards the particles change density and flux by their movement and calculation of fields again take place.

This code initially was developed for gyrotrons and was tested for laser-induced plasmas recently. Details on implementation, computation and recent results are given in [31].

4. Simulations and post-processing

The preceding chapters provided underlying theory and simulational background. This chapter is about main developments and results of simulations obtained. The first section includes results on homogeneous radiation experiments where the irradiated area contains only a few dozen of elementary cells. First aluminium samples of different depths were irradiated to scan the range of fluences over two decades and to compare RES- with TTM-model. This section is followed by a description of script files written in linux shell scripting language being capable of calculating the wanted parameters for aerospace engineering from IMD output files. Also the interface to PICLas code is given by scripts. Finally, computer ablation experiments for aluminium are compared with regard to ablation depths, thermal conductivity and other output values, especially specific impulse and impulse coupling coefficient. In the last section inhomogeneous laser irradation of bigger aluminium samples is discussed. Whenever VLL simulations are under discussion, figures were either directly provided by or created with assistance of S. Scharring [32].

4.1. Homogeneous irradiation

4.1.1. Determination of Parameters

In table 4.1 the main parameters of a recent laser ablation experiment in the laboratory at DLR are given. The maximum energy is not of interest for simulations but added for completeness, the beam waist plays a role in section 4.3. Additionally, the pulse duration is an important laser input parameter, introduced in IMD via equation 2.42 with parameter σ_t. For TTM simulations also material parameters are needed, given in table 4.2.

Table 4.1.: Laser parameters of a recent laser ablation experiment at the DLR using a microchip laser

Maximum energy	Wavelength	Spot diameter at the target	Fluence	Pulse duration
E_{max} [µJ]	λ [µm]	ω_0 [µm]	Φ [J/cm²]	t_{pulse} [ps]
80	1.064	30	$3 - 10$	495

Furthermore, material parameters for the MD systems are needed, interactions were simulated through EAM-potentials. For aluminium, the glue potential of F. Ercolessi and J. B. Adams was used [20]. It was already under proper testing at ITAP [23]. Crystal structures were created with the program **make_config**, the metal being fcc structured with a lattice constant of 4.0513Å.

Table 4.2.: Material parameters for heat conduction in TTM-model (IMD units in brackets)

Material	Electron heat capacity coefficient γ [$\frac{J}{m^3\ K^2}$]	Electron thermal conductivity K [$\frac{J}{K\ m\ s}$]	Electron-phonon-coupling constant G [$\frac{J}{s\ m^3\ K}$][1]
Aluminium	135 (0.11305)[2]	235 (17.33) [3]	$5.69 \cdot 10^{17}$ (0.0004196)[4]

[1] also referred to as κ, here G is chosen due to the parameter declarance in IMD

[2] [26]

[3] [33, p. 759]

[4] [34]

First, a crystal of desired size was created and equilibrated to a desired temperature. After equilibration of the first aluminium samples at $T \approx 300$ K, ablation experiments were started over a wide range of fluences and pulse durations, initially orientated with regard to the DLR laser in a linear scaling behaviour of σ_e and σ_t. For comparison see figure 4.1, red crosses represent the used fluences and pulse durations, the blue cross stands for the laboratory laser. As can be seen the simulated values scale linearly, so an increase of an order of magnitude in pulse duration results in an increase of an order of magnitude in fluence. The simulated values are also given in table A.1 in Appendix A.2. In simulations just the "effective fluence" σ_e, hence the fluence directly bringing in energy on the surface, can be considered. Reflectivity is

not taken into account in any way. This will be discussed in subsection 4.1.5 in detail. For the Lambert-Beer law the penetration depth was set to $\mu = 8\ nm$ [23].

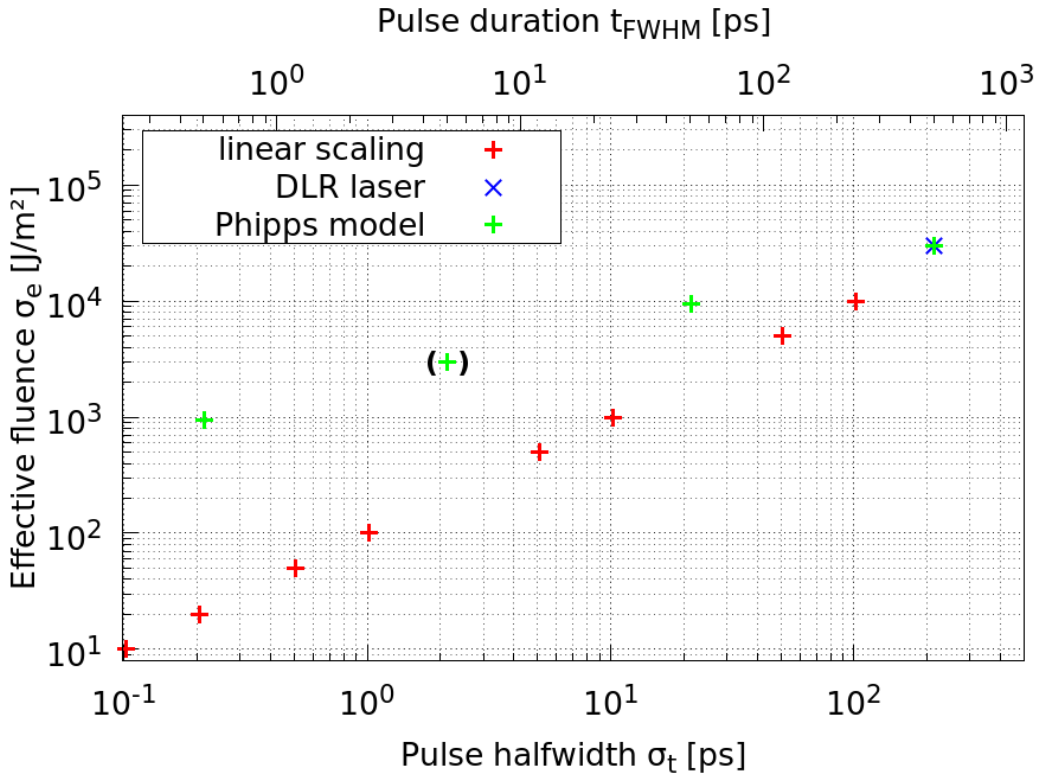

Figure 4.1.: Fluence range of simulations (also tabulated in Appendix A.2)

The green points follow a formula of Phipps for the estimation of the impulse coupling coefficient [35, p. 616]:

$$c_m \sim \left(I\,\lambda\,\sqrt{\tau}\right)^{-1/4} \tag{4.1}$$

Under the assumption $\lambda = const.$ one gets

$$I_1\,\sqrt{\tau_1} = I_2\,\sqrt{\tau_2} \tag{4.2}$$

$$\sigma_{e1}\,\frac{\sqrt{\sigma_{t1}}}{\sigma_{t1}} = \sigma_{e2}\,\frac{\sqrt{\sigma_{t2}}}{\sigma_{t2}} \tag{4.3}$$

$$\sigma_{e2} = \frac{\sigma_{e1}}{\sqrt{\sigma_{t1}}} \cdot \sqrt{\sigma_{t2}} = \frac{3\ J/cm^2}{210\ ps}\ \cdot \sqrt{\sigma_{t2}} \tag{4.4}$$

for the intensities and pulse durations, hence for the effective fluences. If for σ_{t1} (τ_1) and σ_{e1} (I_1) ablation occurs the calculation of σ_{t2} (τ_2) and σ_{e2} (I_2) for another configuration is possible. The formula of the impulse coupling coefficient was determined by Phipps's group from ablation experiments with ns- and ms-pulse lasers. The simulation at $\sigma_t = 2$ ps (in brackets) was not performed, but at this pulse duration fluences were varied in another way (cf. section 4.2.3).

4.1.2. Simulation setup

For clarification of the geometry compare figure 4.2. The samples always were irradiated in x-direction in which they had their greatest extent. The surface of the sample was usually held quadratic, in y- and z- direction periodic boundary conditions were applied. Although the figure and following ones show grey spheres as is just a common convention of visualisation, they represent point particles that interact via the introduced potentials.

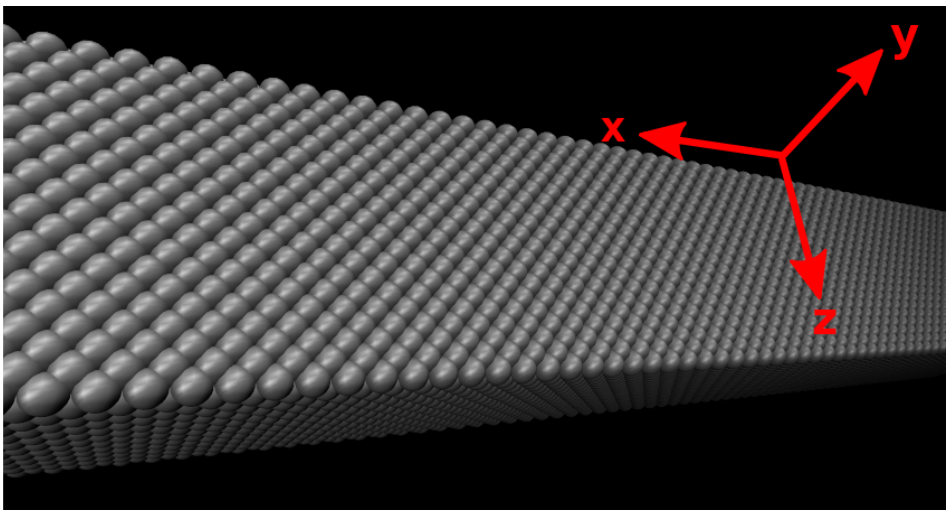

Figure 4.2.: Geometry conventions

First test runs not discussed in detail here included samples with just 10 x 10 $\approx$ 100 elementary cells building the area ($A \approx 56$ x 56 Å^2) perpendicular to the irradiation direction. They showed unphysical behaviours as a "plate" of atoms was expelled from the surface (compare figure 4.3). There was not enough space for cluster or fluid drop formation and the initial configuration had a big influence. Fluctuations in the velocity distribution directly are projected onto the evolution in time in these cases,

so following experiments used a few dozen elementary cells in y- and z- direction, resulting in a better distribution of energy over the whole sample.

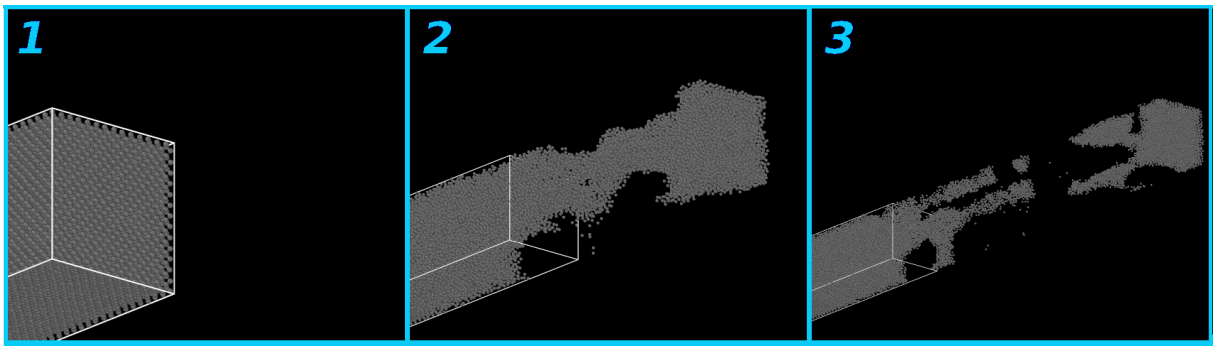

Figure 4.3.: Three screenshots of a simulation with 25 elementary cells, zooming out over time. Block formation can easily be seen in (2) and (3).

The simulations were done mainly on four different systems, an Intel Xeon Processor X5570 (Nehalem-EP) with 8 threads (4 physical) running at 2.93 GHz, refered to as CPU (1), an Intel Xeon Processor X5670 (Nehalem-EP) with 12 threads (6 physical) running at 2.93 GHz , referred to as CPU (2), an Intel Xeon Processor E5-2620 (Sandy Bridge EP) with 12 threads (6 physical) running on 2.0 GHz, referred to as CPU (3) and an Intel Xeon Processor E5-2670 (Sandy Bridge EP) with 32 threads (16 physical) running on 2.6 GHz, referred to as CPU (4) in the following.

Table 4.3.: Extracts of test run simulations

σ_t	model	computation time [s]	simulation time [fs]	# atoms	CPU	# threads
200 fs	TTM	359318 (4 d 3h)	50900 (50 ps)	14151200	(1)	8
5 ps	RES	420528 (4 d 19 h)	50900 (50 ps)	14151200	(1)	8
5 ps	TTM	502500 (5 d 19 h)	50900 (50 ps)	14151200	(1)	8
50 ps	TTM	1823820 (21 d)	311508 (311 ps)	3750000	(2)	12
100 ps	RES	3629760 (42 d)	701605 (701 ps)	3750000	(1)	8
100 ps	TTM	2480700 (28d17h)	68920 (689ps)	3750000	(2)	12
2.1 ps	TTM	183600 (2d3h)	4072 (40 ps)	3750000	(4)	8
210 ps	RES	508980 (5d19h)	4632 (45.5 ps)	37500000	(4)	16

Two main systems, one with around $14.15 \cdot 10^6$, the other with $3.75 \cdot 10^6$ atoms were simulated in the first test runs. In table 4.3 a brief overview of scaling parameters

concerning computation is given. The statistics were not always done at the end of the simulations, which is the reason that simulation times do not always coincide with the values of table A.1. The simulations are classified by their pulse halfwidth σ_t, the used model (TTM or RES), computation time in seconds and days on CPUs, the simulated time in fs and ps, the number of atoms, used CPU and threads. The simulation times cover at least a minimum of 3 σ_t, so the pulses passed through already before the simulation end. Sometimes simulations were aborted by the user. Typical simulation times on available standard calculation nodes need times of around $10 - 20\ ps/day$, depending on the number of cores. It can be clearly seen that the TTM model on the same architecture needs longer than RES simulations.

4.1.3. Simulations with linear pulse parameter scaling

In the following figures the density evolution in time are shown. On x-axis the distance from the surface is plotted, positive values stand for positions laying deeper inside the sample, negative values stand for positions outside the initial sample. The density distribution was calculated through scripts that used the density standard output provided by IMD (if the flags **dist_dens_flag** and **dist_int** are set). It was set the way that the density was calculated by dividing the sample in x-direction in slices and using the number of particles within these. The laser maximum in time is always set to 0 ps in the density plots. The first experiments in the 100 fs regime showed density waves that propagated through the sample (cf. figure 4.4, left).

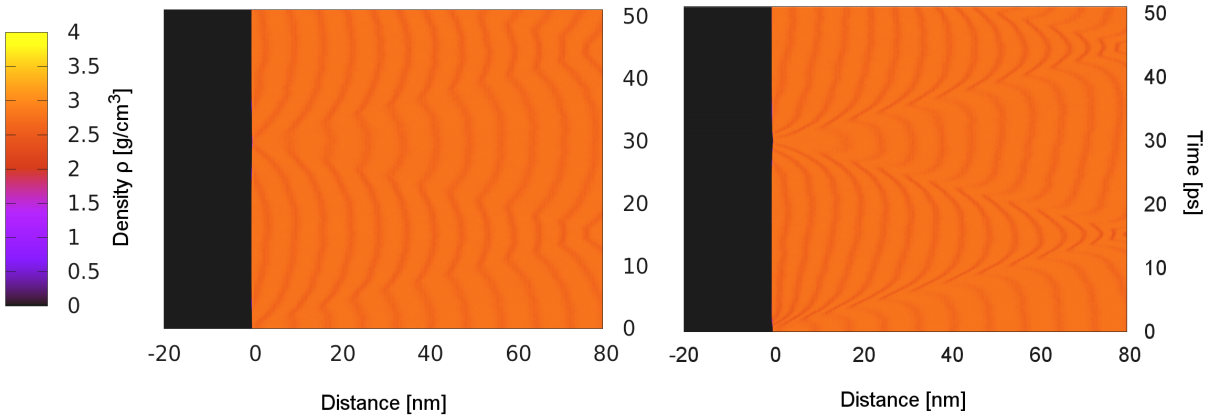

Figure 4.4.: Density plots for $\sigma_t = 100$ fs, $\sigma_e = 10\ J/m^2$, TTM (left) and $\sigma_t = 200$ fs, $\sigma_e = 20\ J/m^2$ TTM (right)

They started when the energy of the short pulses was coupled in by distortion of a few atoms at the surface. No phase transition occured for the first three laser experiments given in figure 4.1 by the red dots, independent of the used model (RES or TTM). Density waves were reflected at the back of the samples and ran between the two surfaces on the left and right with a velocity of around

$$\frac{80\ \mathrm{nm}}{14\ \mathrm{ps}} \approx 5.71\ \frac{\mathrm{km}}{\mathrm{s}} \quad , \tag{4.5}$$

which lies in the order of the velocity of sound waves in aluminium ($v_{sound} \approx 6.42$ km/s at 300 K, longitudinal waves, [36, p.14-36]).

The density of molten aluminium follows from [37]:

$$\rho\,(T) = 2377.23 - 0.311 \cdot (T/\mathrm{K} - 933.47)\ \frac{\mathrm{kg}}{\mathrm{m}^3} \tag{4.6}$$

It lies in the range of $2.3 - 2.39\ \mathrm{g/cm^3}$ for $T \in [900\ \mathrm{K}, 1190\ \mathrm{K}]$. The critical density, where gas and liquid phase are not separable anymore, lies in the range of $\rho_c = 0.28 - 0.79\ \mathrm{g/cm^3}$ [38].

At a pulse halfwidth of $\sigma_t = 1$ ps ($t_{FWHM} \approx 2.3548$ ps) and an effectice fluence of $\sigma_e = 100\ \mathrm{J/m^2}$ a phase transition at the surface occurs. A stable liquid layer exists which is disturbed by density waves reflected from the right surface (cf. figure 4.5, right). However, no ablation occurs.

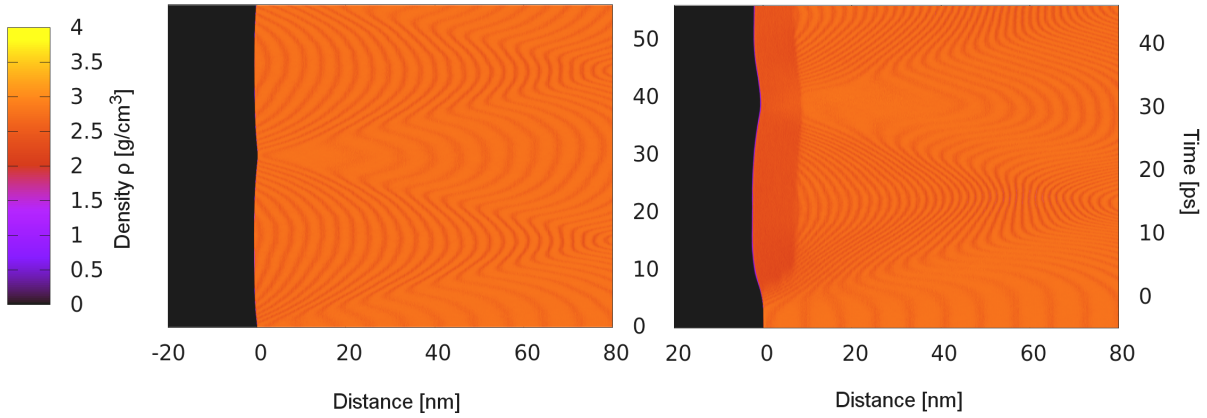

Figure 4.5.: Density plots for $\sigma_t = 500$ fs, $\sigma_e = 50\ \mathrm{J/m^2}$, TTM (left) and $\sigma_t = 1$ ps, $\sigma_e = 100\ \mathrm{J/m^2}$ TTM (right)

Another phase transition to the gas phase firstly occurs at $\sigma_t = 5$ ps and $\sigma_e = 500$ J/m², both for the RES- and the TTM-model (figure 4.6). In the range of a few penetration depths ($\mu \approx 8$ nm) the material is molten and a gaseous phase is expelled into the vacuum on the left. The reflected density wave after ≈ 25 ps disturbs the solid-liquid and the liquid-gas interface. The two models show clear differences in behaviour of the energy distribution by heat transport mechanisms and the resulting evolution of phase transitions, ablation and spallation. It can be seen that the simulated metal plate of 80 nm thickness is completely molten after 20 ps in TTM case. The melting takes place later than in the RES-model because the electronic system has to transfer the heat to the lattice over a longer time instead of influencing the velocities of the atoms directly as in RES-model. The heat is conducted over the whole sample and causes ablation of a fluid layer on the front (left surface) and spallation of a liquid-gas phase on the back (right surface).

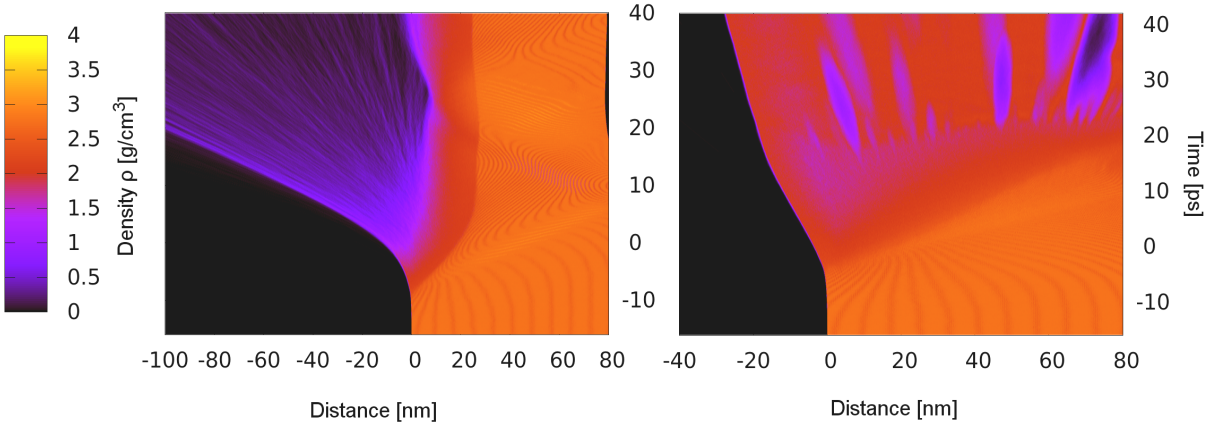

Figure 4.6.: Density plots for $\sigma_t = 5$ ps, $\sigma_e = 500$ J/m², RES (left) and TTM (right)

The evolution into vacuum on the back can not be seen because the distribution parameters in IMD were not set properly. The main mechanisms of the TTM-modelled system on the right of figure 4.6 take place after the main mechanisms of the RES-modelled one, which stays stable neglecting the density waves which would not occur in samples of bigger extent in x-direction. Spallation is due to the density waves, without disturbance on the right it would not occur at this magnitude. The wave is reflected at around 10 ps and hits after reflection the liquid phase at around 20 ps, leading to the expulsion of the liquid-gas phase at $60 - 80$ nm. In principal, the same effects as for $\sigma_t = 5$ ps and $\sigma_e = 500$ J/m² for RES- and TTM-model can be seen for $\sigma_t = 10$ ps and $\sigma_e = 1000$ J/m². In the latter case (compare figure 4.7) reflection of

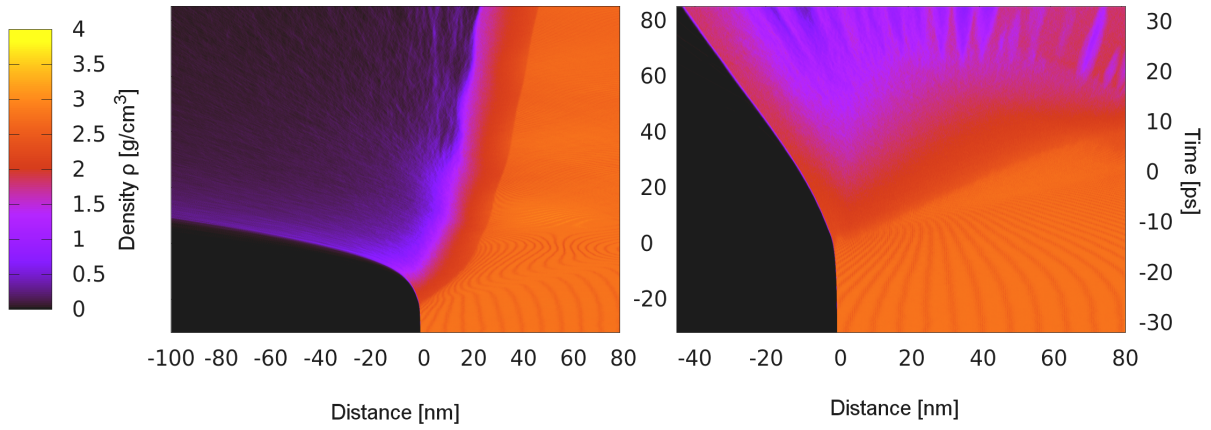

Figure 4.7.: Density plots for $\sigma_t = 10$ ps, $\sigma_e = 1000$ J/m², RES (left) and TTM (right)

density waves can be seen more often in RES-model since the higher energy lets the material melt deeper, so the phase interfaces are closer to the backside of the sample on the right.

The TTM simulation shows a partial vaporisation of the sample, a liquid front is expelled from the surface beforehand. This can be explained by not so fine-tuned simulation box parameters, no space was left between the surface of the sample and the simulation box. All simulations discussed here were run in a simulation box that was completely filled by the sample. This is important in y- and z-direction for periodic boundary conditions, since the atomic interactions are calculated by the influence of their periodic neighbours. When applying periodic boundary conditions, the distance of the atoms in y- and z- direction has to be half of the characteristic radius of the potentials. In the front (on the left), however, it is important to leave some space since the surface of the sample may enlarge under long laser pulses. If the surfaces extents upon the box boundaries, the interactions of surface atoms are no longer calculated. No further energy is coupled in by the laser and, in TTM case, no TTM calculations are done. Instead all atoms that surpass the box boundaries keep their velocity as a constant. The laser energy always is coupled in from $x = 0$ following Lambert-Beer's law along the positive x-axis. Vaporisation takes place beyond an expelled liquid zone that already has a high enough velocity to leave the surface (from 5 ps on). The back spallation shows the same effects induced by the reflected density wave as in the simulation with $\sigma_t = 5$ ps and $\sigma_e = 500$ J/m².
Simulating longer pulses with $\sigma_t = 50$ ps, $\sigma_e = 5000$ J/m² and $\sigma_t = 100$ ps, $\sigma_e = 10000$ J/m² leads to similar conclusions in the RES-model as stated before.

The laser energy melts the surface in the order of a few penetration depths, on the irradiated surface a gas phase develops that leaves the sample with velocities of $\approx 5000 \pm 1600\,m/s$, cf. figure 4.8, left and 4.9, respectively.

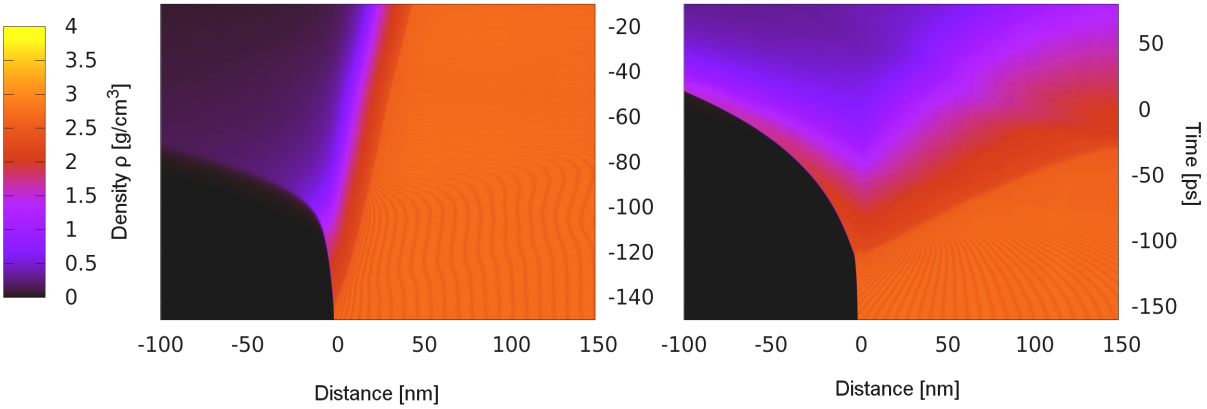

Figure 4.8.: Density plots for $\sigma_t = 50$ ps, $\sigma_e = 5000$ J/m², RES (left) and TTM (right)

The TTM-modelled simulations, however, show interesting features. While it seems that the evolution of evaporation just goes on for $\sigma_t = 50$ ps, $\sigma_e = 5000$ J/m² and the sample completely ends in the gas phase during laser irradation, the surface of the sample with $\sigma_t = 100$ ps, $\sigma_e = 10000$ J/m² shows a stable liquid phase of aluminium. The reflected density wave has a much slower velocity in liquid aluminium but disturbs the fluid surface at around 110 ps after pulse peak. Such a long pulse shows an energy incoupling that is temporally distributed in a way that the liquid aluminium can not form a gas phase. Due to the longer pulse time, the energy transfer per time step is too low to excite the material such that it heats up over ablation threshold. Of course, also the simulation parameters have to be taken into account. Since the energy after extension of the surface is coupled in deeper into the sample, the surface atoms are not excited any more.

4.1.4. Simulation with non-linear pulse parameter scaling

After the first test runs, the Phipps model was chosen to simulate systems being better comparable with DLR experiments. All simulations are done with the TTM-model since the rescaling model provides unphysical results! In the laboratory usual crater

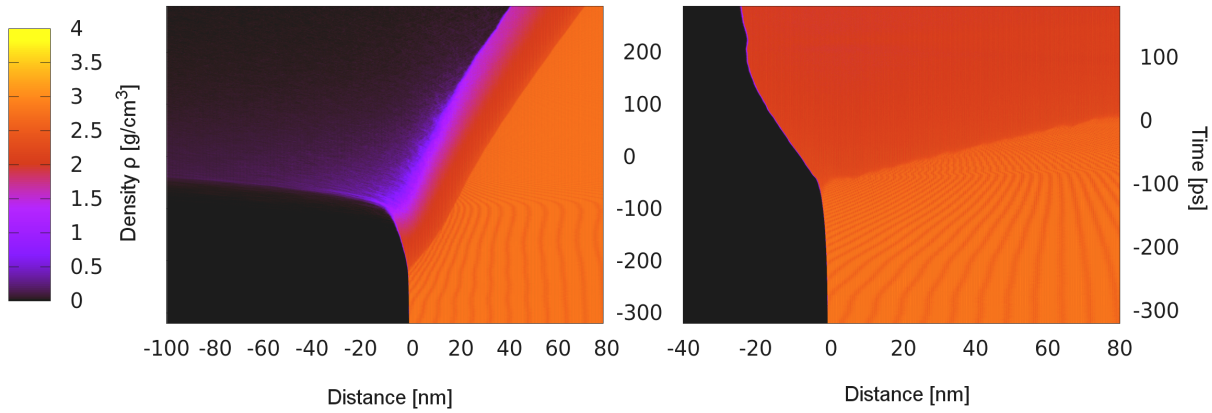

Figure 4.9.: Density plots for $\sigma_t = 100$ ps, $\sigma_e = 10000$ J/m², RES (left) and TTM (right)

depths lie in the µm range [39], which never would be achieved by this model, since the melting depths just lie in the range of multiple penetration depths and therefore in the nm range. In figure 4.10, the density plots of a $\sigma_t = 21$ ps laser pulse and a $\sigma_t = 210$ ps laser pulse are given. The latter refers directly to the DLR laboratory laser but was stopped before even the pulse maximum time was achieved. Getting the whole time of the whole pulse would have taken weeks. The sample itself is completely melted after 200 ps and is just too small in x-direction, so a simulation with a deeper sample would lie within time scales of months.

The shorter pulse with $\sigma_t = 21$ ps would also have melted the whole sample and maybe have led to spallation if a special feature of IMD was not active in this simulation. It is possible to introduce an artificial damping term over parts of the sample. This was implemented to supress reflecting density waves that disturb the evolution of the surface properties during ablation [23], since surface evolution often is of interest. Here the last thirth of the sample on the right was a damping layer. As can be seen the energy drain of the system surpresses density waves and melting. This simulation physically is not right in any kind but illustrates what else can be done with IMD. Since the DLR laser pulse time was not possible to be simulated in proper time, further results just take into account pulse halfwidths of $\sigma_t = 2.1$ ps and 21 ps ($t_{FWHM} \approx 5$ ps and 50 ps). Since future experiments at DLR might cover shorter pulses in the 10 ps regime direct comparisons will be possible.

VLL simulations estimated melting depths of ~1 µm for $\sigma_t = 21$ ps, $\sigma_e = 9490$ J/m², so a deeper sample of aluminium was created and equilibrated. Its extent in x-direction was 1.5 µm, in y- and z- direction 20 nm and included $37.5 \cdot 10^6$ particles. In one day

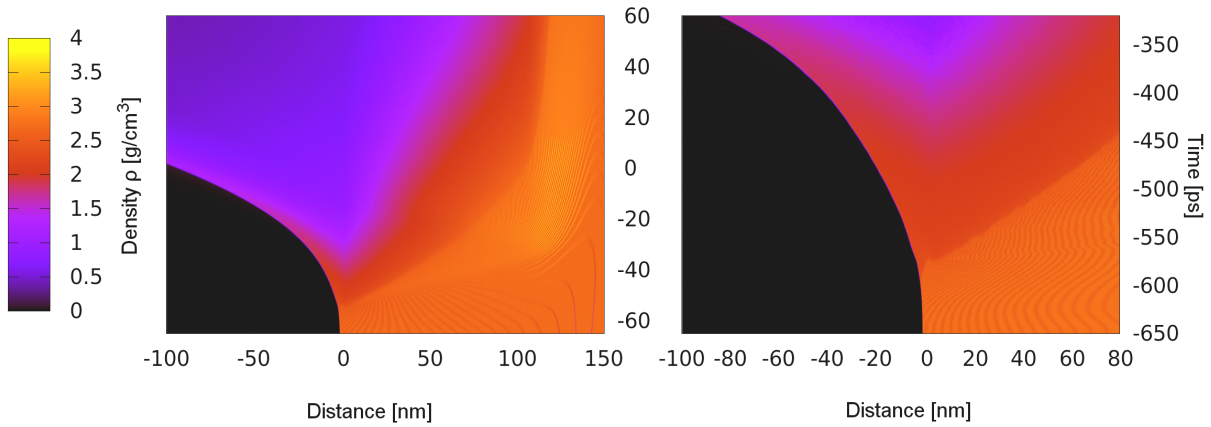

Figure 4.10.: Density plots for $\sigma_t = 21$ ps, $\sigma_e = 9490$ J/m², TTM (left) and $\sigma_t = 210$ ps, $\sigma_e = 30000$ J/m² TTM (right)

on CPU (3) only 2.97 ps could be simulated, which was done for 11 weeks. The whole simulation time then was ≈ 228.4 ps. The density evolution is given in figure 4.11. The surface begins to melt approximately 2 σ_t before the laser maximum, before the input energy already gives rise to a density wave which travels to the back of the sample. A region, denser than unaffected aluminium, is followed by a region as dense as solid aluminium. The density wave represents a standard textbook longitudinal density

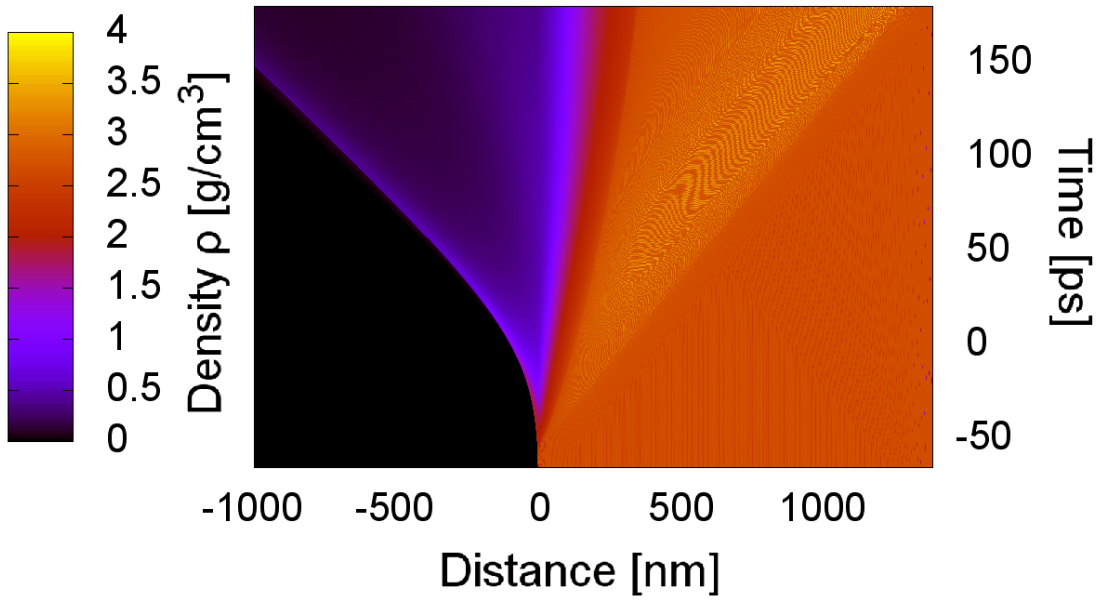

Figure 4.11.: Density plot for $\sigma_t = 21$ ps, $\sigma_e = 9490$ J/m², TTM

wave. Closer to the surface a phase transition to liquid follows. On the surface the melt is vapourized and expelled from the sample. When travelling away from the surface the material gets less dense due to gas expansion.

The simulation box in this simulation also included the whole sample as in the simulations before, so surface particles leaving the box on the left directly were expelled because the potentials were not calculated anymore. This explains the layer ablation from time -40 ps on. In this simulation, also a damping ramp was applied since the VLL simulations showed ablation depths of 1 µm. It was set on the last 15 % of the sample on the right, which explains why its direct effect can not be seen in the density plot of figure 4.11. However the energy drain can be noticed in the temperature distributions given in figure 4.12. The times correspond to the beginning of the simulation, the laser maximum occurred after 65 ps. On the left picture, temperature distributions over the sample are given for four times at the beginning of the simulation, i.e. 0 ps, 0.2 ps, 1.2 ps and 10.4 ps. Electronic temperatures are given by lines, the temperature of ions by points. Since both values are calculated within finite cells, both have non-continuous shapes. However for distinguishing this representation for electrons is chosen. As it can be seen, the initial configuration has a temperature of 322 K, being equally distributed over the whole sample. After 200 fs the energy drain at the back (on the left) can be clearly seen already, the ramp starts at 1275 nm. After 1.2 ps the atoms in the ramp zone have almost lost their kinetic energy and therefore the sample has a temperature close to 0 K. The fraction zone also effects the atoms that are near to it, but are not damped themselves. It can be seen that the zone of low kinetic energy wanders in x-direction towards the surface (on the left). However, this does not affect the surface itself for a long time span, although it drains energy out of the system in an unphysical way. However, for big samples this does not play a big role within these time scales.

Looking at the evolution of temperatures of the surface atoms on the left, the electronic excitations can be seen to forego the lattice's reactions. The laser field couples to the electrons, resulting in a steep rise of electron temperature. The ionic temperature follows due to electron-phonon coupling. In figure 4.12 on the right the distributions are given for later simulation times. After ~100 ps of simulation time the pulse peak passed through and $3/2\ \sigma_t$ have passed since that, so most of the energy is put into the electronic system already (red curve). The electrons of surface atoms have a maximum temperature of ~34500 K, the ions are close to that temperature already. From

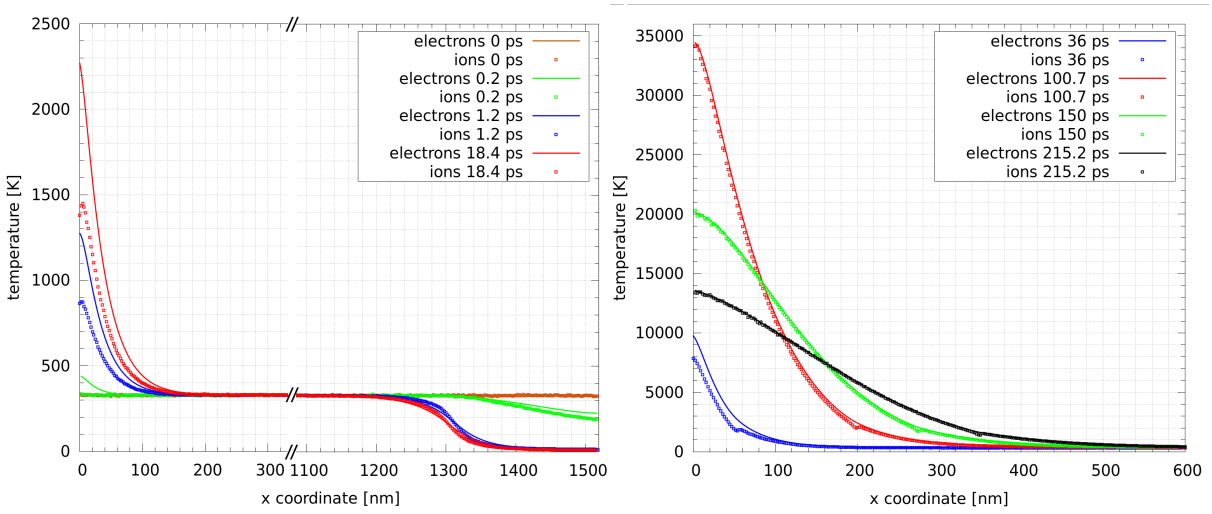

Figure 4.12.: Temperature plots for $\sigma_t = 21$ ps, $\sigma_e = 9490$ J/m², TTM

the right plot in figure 4.13 it can be seen that at ~100 ps the surface atoms have a temperature deviation of less than 5 percent in relation to the electronic temperature. The further time evolution of the electronic and ionic system shows a steady adaption of temperatures over the whole sample.

The relative temperature difference shows an interesting behaviour. As the laser has a symmetric temporal distribution, the relative temperature difference distribution should also show a symmetric behaviour. However, on left and right of the occuring wandering difference peak the shape is not symmetric. There are two possible explanations. On one hand, the extension on the left, which can not be seen because the distribution statistics were set by the user to start from the surface to the inner sample, can redistribute the energy on the left due to phase transitions. Different parts of the energy can be absorbed by material of different densities. On the other hand, a side effect of the simulation box which might be set too tight is supposed to be the main problem here. Due to its unphysical behaviour of layer ablation, which can be seen in the density plot, surface layers are cut and carry thermal energy away from the sample.

In further time evolution the thermal relaxation goes on and, except for the wandering peak, the electronic and ionic systems differ less than 2.5 % in temperature over half of the sample shown in plot after 217.7 ps simulation time (152.7 ps after laser pulse maximum). The right end of the sample is not shown because of the unphysical

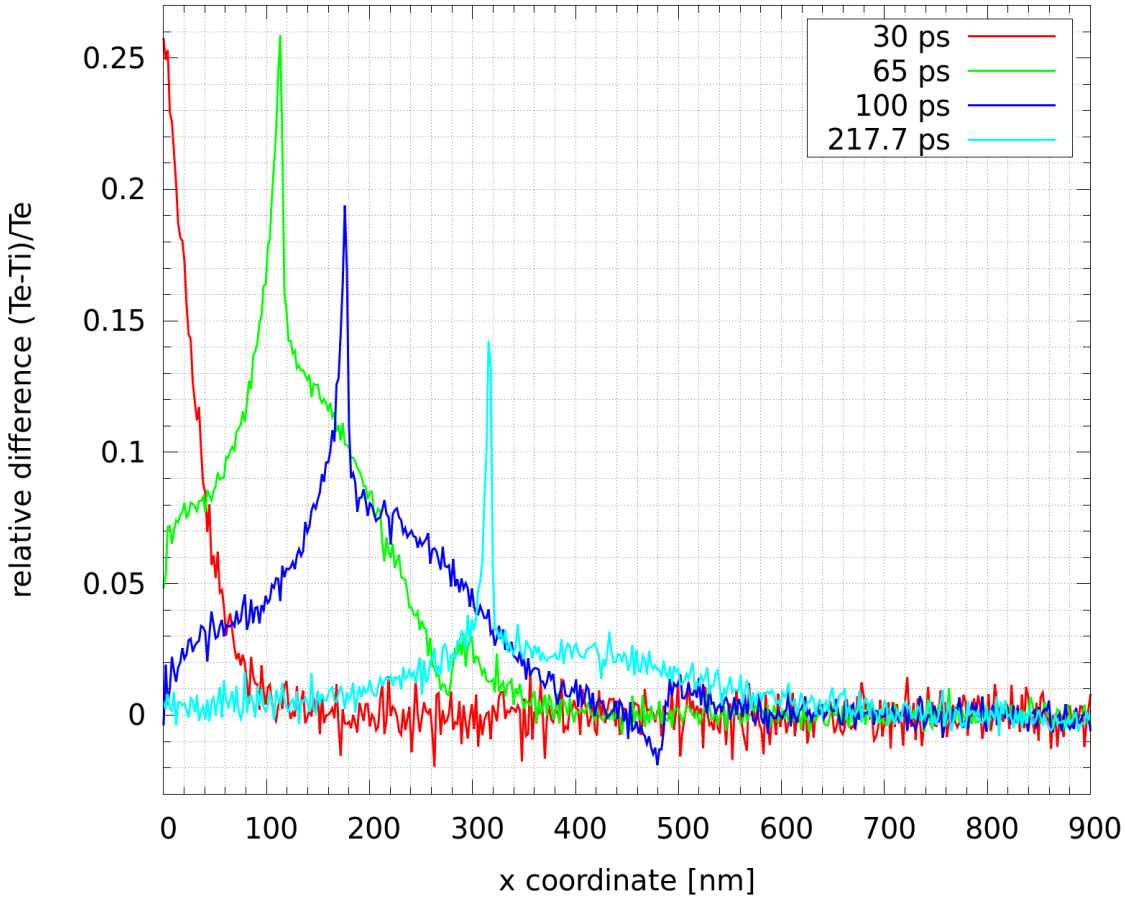

Figure 4.13.: Relative difference between temperatures at different time steps (right) at $\sigma_t = 21$ ps

behaviour due to the damping layer which is artificially introduced, causing mighty jumps in the temperature difference.

A brief discussion is given on a simulation at $\sigma_t = 2.1$ ps and $\sigma_e = 5.94$ J/cm². The density plot is given in figure 4.14 (right). Due to the lack of time at the end of studies, the overall simulation time is much shorter than before. The influence of a proper set by simulation box can be seen on the surface (on the left). The material is expanding over the initial surface and still energy of the laser is coupled in, since the phase transitions go forth, contrary to the simulation of the 21 ps pulse (cf. figure 4.11), where a layer was expelled that had its phase transition after travelling away $50 - 100$ nm from the surface. Again, a density wave can be recognized, travelling into the sample. However, there are much denser regions than in the simulations with shorter pulse durations. On the surface, phase transitions from liquid to gas occur.

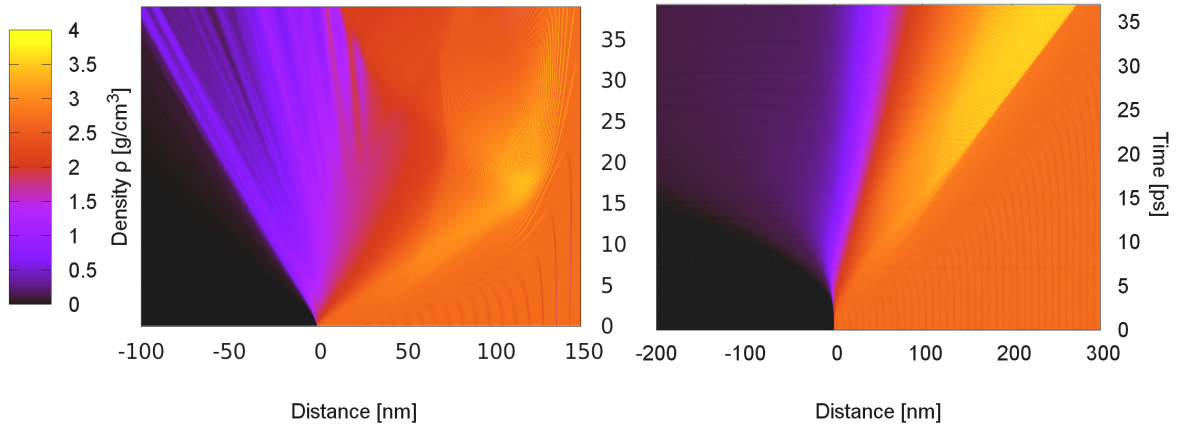

Figure 4.14.: Density plots for $\sigma_t = 210$ fs, TTM (left), and for $\sigma_t = 2.1$ ps, TTM (right)

Following Phipps's formula, another simulation was performed for $\sigma_t = 210$ fs. Again a damping ramp was introduced in this simulation. The simulation parameters at $\sigma_t = 2.1$ ps were not chosen following equation 4.2, but were configured to describe test runs for aerospace parameters in section 4.2.3 at different fluences. The simulation for $\sigma_t = 210$ fs shows ablation, cf. figure 4.13 (left). It follows that the Phipps formula can be used to roughly predict ablation fluences when known for one certain configuration even in these time scales. Evolution of specific impulse and impulse coupling coefficient follow in section 4.2.3.

4.1.5. Target reflectivity

Another discussion is worthwhile, i.e. the impact of reflectivity on simulations. Initially, IMD was developed for studies of materials under mechanical and thermal strain. Also fs-pulse laser ablation was taken into development. However, ultrashort laser pulses will change the materials properties but will not get affected in their time and space evolution since the processes changing materials parameters start after the irradiation itself. This is not the case anymore for longer pulses, e.g. in ps-regime, as discussed in this thesis, or even ms-pulses. The IMD code in its recent implementation does not take into account for changes in optical properties during ablation. This means that the reflectivity of a sample is considered as a constant. In figure 4.15 on the left the time evolution of reflectivity of a VLL simulation is given. The irradation follows the same laser parameters as the before discussed pulse with $\sigma_t = 210$ ps.

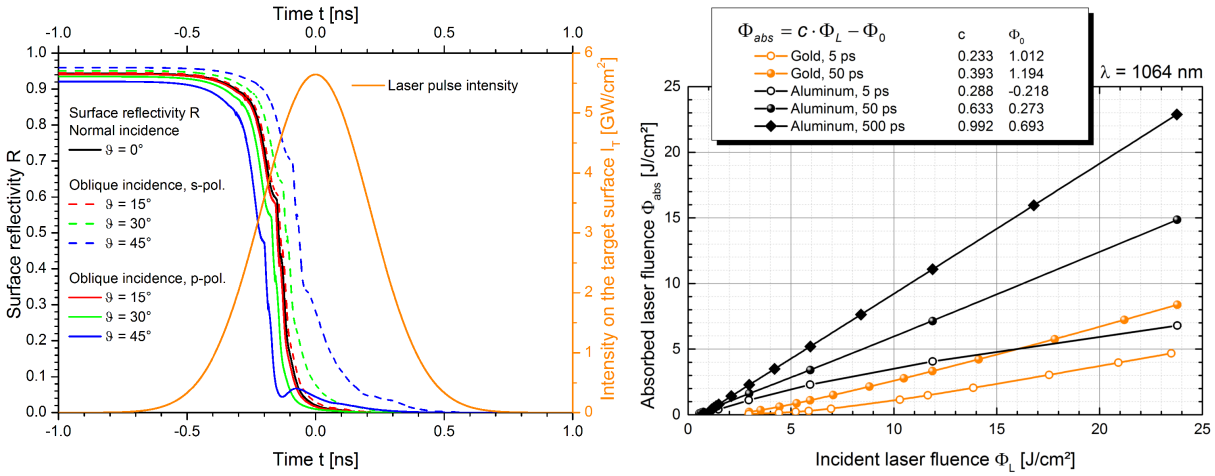

Figure 4.15.: Reflectivity evolution in time of a VLL simulation, $\sigma_t = 210$ ps(left) and effective fluence versus incidence fluence for different laser parameters (right), VLL simulation, [32]

Around the pulse maximum, under most incidence angles the reflectivity drops to zero. From this time on, the laser energy is completely absorbed by the surface atoms (which are partially gaseous and liquid to a certain depth) and the IMD simulation can be compared directly. However, the time before that reflectivity drop is not simulated in a physical correct way by the provided IMD simulations. Instead, always the whole energy is coupled in. Of course, there are issues where the experimentalist can choose a combination of laser wavelength and material with almost hundert percent absorption of irradiation. Nevertheless, the comparison here is just possible with the described experimental laser due to outer cornerstones not being open to influence. As further VLL simulations show, the absorbed laser fluence is even lower for shorter

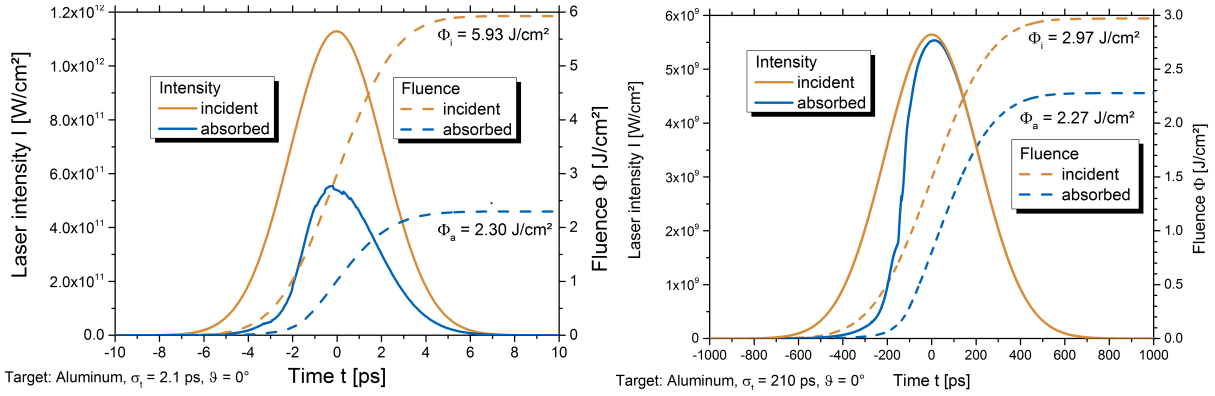

Figure 4.16.: Absorbed laser intensities for $\sigma_t = 2.1$ ps (left) and $\sigma_t = 210$ ps (right), VLL simulations [32]

ps-pulses. In figure 4.16 another representation of absorbed laser light is given. The two figures show the intensity of incident and absorbed irradiation VLL simulations equivalent to IMD laser pulses referred to by $\sigma_t = 210$ ps and $\sigma_t = 2.1$ ps. Although it seems a problem in figure 4.15 (left), most of the energy of the longer laser pulse is absorbed by the sample. This is due to the fall of reflectivity during the irradiation, which reaches 50 percent at a time when only a small part of the laser energy is absorbed yet, i.e. around 25 percent (cf. figure 4.16, left). However, in case of the pulse at $\sigma_t = 2.1$ ps there is a huge difference between incident and absorbed laser energy. The absorbed laser energy here means the part of the incident electromagnetic waves that are not reflected and yield to melting and ablation mechanisms. It is given directly from simulational data, calculated from the ingoing and outgoing parts of the electromagnetic waves.

Another representation is given in figure 4.15 on the right. The absorbed fluence is plotted versus incident fluence, this time for a variety of pulse durations. Also gold is given as comparison. Each point stands for an evaluated VLL simulation, simulated for a few nanoseconds. Simulations of that kind roughly need half a day of simulation time. They show an interesting behaviour, i.e. they scale linearly. Some of the points for lower fluences represent simulations where no ablation occured. It is highly surprising that for both ablation and melting phenomena the same scaling between incident and absorbed laser energy holds. The mechanism of absorption seems to be the same in both cases. That is not the only surprising fact. These relation also holds for aluminium and gold, two materials that differ in most of the important material parameters like electron-phonon coupling, heat conductivity, atomic mass and thermal conductivity. However, the slopes of proportional functions differ. While for aluminium it is next to 1 for the long pulses at $\sigma_t = 210$ ps ($t_{pulse} = 500$ ps), it is about 0.633 for 21 ps-pulses ($t_{pulse} = 50$ ps) and even lower for 2.1 ps ($t_{pulse} = 5$ ps). In the two latter cases, the conclusions to be made for IMD simulations can not be connected to experimental data directly. Under the assumption that with Phipps's formula the shorter pulses can be compared to the laser, still the reflectivity behaviours shown here are not used in IMD simulations yet. Thus, for comparison of IMD simulations with shorter pulses, the conclusions have to be scored carefully. However, in the 210 ps-regime, conclusions are almost directly comparable. For gold with the same pulse parameters as for aluminium, the slopes are much smaller at $\sigma_t = 21$ ps, while for shorter pulses they are comparable.

4.2. Post-processing of IMD simulation data

4.2.1. Interface to PICLas

In the current implementation of the PICLas code the committed files shall include the left and right coordinates in x-direction of a cell, for which a density and a temperature is given. IMD can write out distribution files of density and kinetic energy, as well as in the TTM model it can distinguish between electronic and ionic temperature. Density plots have already been discussed in section 4.1. To write a distribution the user has to specify some variables in the parameter file of IMD, i.e. the left lower corner (**dist_ll**) and upper right corner (**dist_ur**) of the box in which the values are calculated out of particle information. This can be bigger than the simulation box, both sizes are uncoupled. Also zones of calculation have to be set. The distribution box can be divided into subboxes to get a spatial resolution of density and kinetic energy. As an example, the parameters

dist_dim 500 1 1

subdivide the box in x-direction in 500 slices, whereas in y- and z-direction the complete box is used for statistics. If the values

dist_dens_flag 3
dist_Ekin_flag 3

are set, density and kinetic energy is calculated from particle positions, mass and velocity in the previously defined boxes. The numbers indicate the dimension (also two dimensional simulations are possible). The statistics are not done every time step, but can be set to multiples of time steps via

dist_int 100 ,

here every 100 time steps density and kinetic energy are calculated. The values are written to files with ending **.dens** and **.Ekin**, respectively, containing one column in this case with 500 rows. These files have to be merged into a table for PICLas in the way:

left edge of cell right edge of cell density temperature

Three values have to be given to the script manually, i.e. the line of the surface cell in a **.ttm**- or **.dens**-file, the absolute value of the left lower corner of the distribution box and the beginning of the sample in Angstrom from **.chkpt**-file. The last two values are added and divided by the number of lines for the vacuum on the left, given by the first value. This gives the spacing of x-values Δx. Now successively the cell number n is increased from zero, the left and right edges of each box are given by $n \cdot \Delta x$ and $(n+1) \cdot \Delta x$, which are written to a file **to_PICLas.<timestep>.dat**. Finally, the density and temperature are taken from their distribution files at the actual cell number, which equals the line number n minus the header lines of **.dens**- and **.Ekin**-files. For details, the script is given in Appendix A.1.2.

4.2.2. Aerospace parameters

IMD provides **.chkpt**-files that include a header defining the box parameters followed by lines that continue informations of all particles of the simulation looking like:

atom number type mass x y z vx vy vz Epot eam_rho

It is a listing with rows containing the atom number and the atom type, labelled by a number, the atomic mass in a.u., the x-, y- and z-coordinates in Å, the velocities in x-, y- and z- direction in Å/fs and the potential energy Φ and electron density ρ for EAM calculations. For calculation of the specific impulse and the impulse coupling coefficient the columns 3 (mass) and 7-9 (velocities) are important. As described in section 2.1.2, both aerospace parameters are based on velocity differences. In the script **aerospace.sh** (compare Appendix A.1) first impulses in x-, y- and z-directions are summed up for all particles following equation 2.3. Also the sum over all masses is calculated. After calculation of the absolute impulse $|\mathbf{p}|$ surface widths in y- and z-direction as well as the fluence are taken from the parameter file **laser.param**.

For every checkpoint file afterwards an output file is provided containing all parameters described and the direction vector coordinates. This information also can be used for angular distribution calculations. Followed by the calculation of the specific impulse and the impulse coupling coefficient, where the energy at homogeneous irradiation is given by $E = \Phi \cdot A$ with A being the surface area.

Finally the timestep, impulse coupling coeffient, specific impulse, fluence, area and energy are written to another output file, **DLR.data**. Since this is done for every checkpoint file, in the end, the time evolution of the aerospace parameters is obtained.

One main issue is the selection of the particles belonging to the plume that the described calculations are applied on. Until now, the criterion is that particles with a x-coordinate left from the initial surface are taken into account. Of course, also another x-coordinate than the initial surface position can be set in the now provided script. However it would be better to take velocities into account the way that both the sample and plume particles hold

$$\sum_{i \in plume} p_i = - \sum_{k \in target} p_k \quad . \tag{4.7}$$

This would need a stepwise summing up and testing if the difference

$$\Delta p = \sum_i p_i - \sum_k p_k \tag{4.8}$$

undergoes a critical value, when summing up over i from the ablated surface side and k from the back of the sample, e.g. a threshold that lies in the order of thermal fluctuations at room temperature.

4.2.3. Aerospace study

The output of the script for the aerospace parameters specific impulse and impulse coupling coefficient is discussed in this section. First, the realised simulation at 21 ps already discussed in section 4.1 is observed. Second, simulations at 2 ps for aluminium are discussed.

In figure 4.17 the output of the impulse coupling coefficient is given. The particles that contribute to the calculation have an x-coordinate that lies beyond the left surface given in the density plots. As a comparison the impulse coupling coefficient over time for a pure TTM simulation and three NVE simulations are plotted. These belong to different starting points of simulations, so after 100 ps, 125 ps and 150 ps the checkpoint file of the TTM simulation was further integrated by the standard NVE integrator.

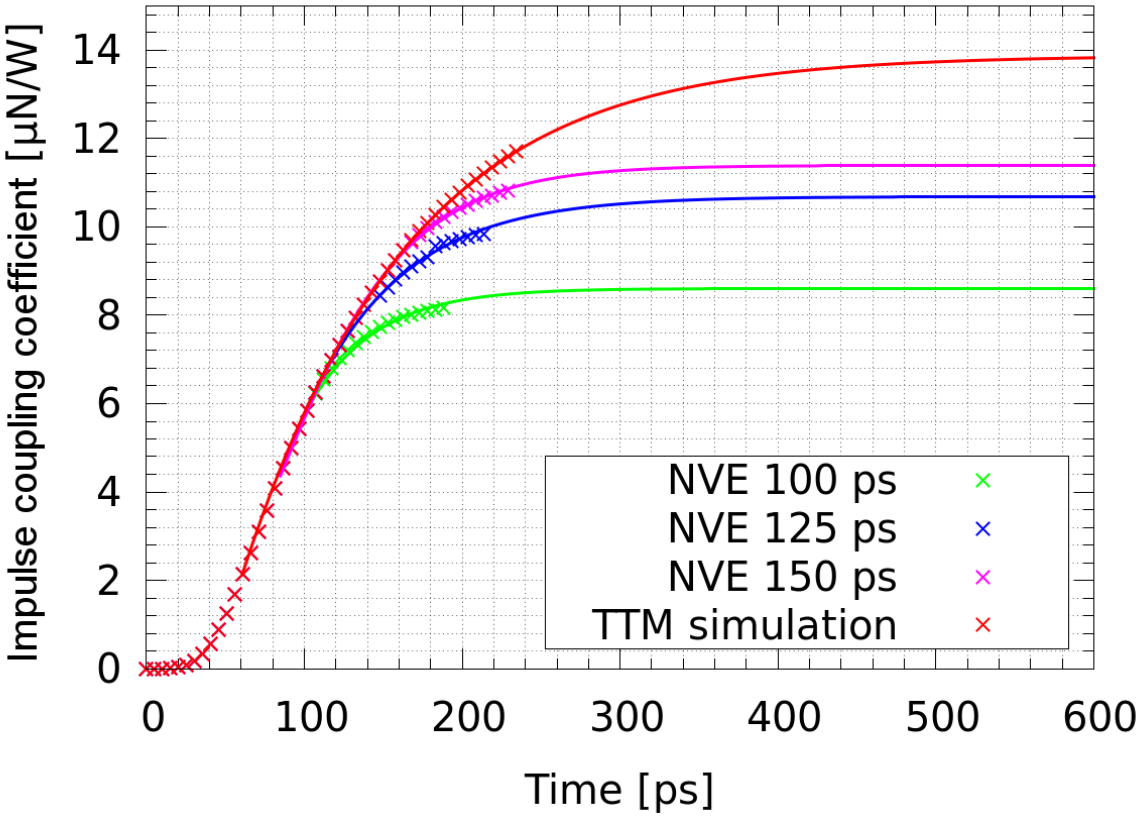

Figure 4.17.: Time evolution of impulse coupling coefficient c_m for simulation of laser ablation of aluminium by a laser pulse with $\sigma_t = 21$ ps

Due to the different temperature distributions of the sample, which then take no further TTM calculations into account, the amount of ablated particles changes. The calculated values were fitted with a function, i.e.

$$c_m(t) = C_1 + C_2 \cdot e^{-t/K_1} + C_3 \cdot e^{-t/K_2} \quad . \tag{4.9}$$

For $t \to \infty$ the value C_1 results, giving an estimate of the specific impulse c_m. The fitting values are given in table 4.5. Also the ratio to the fit of the TTM calculation is given, resulting in better agreement, the later the start of NVE integration was. As it was shown in figure 4.13, the relative temperature difference between electronic and ionic subsystem was less than 5 percent after 100 ps simulation time into a depth of 100 nm from the surface. Still, this does not seem to be a good threshold for further NVE simulations. Unfortunately due to lack of time it was not possible to simulate a NVE simulation after 215 ps simulation time. This seems that it would have been the best choice, since the relative temperature difference is smaller than one percent until a depth of 200 nm. The TTM simulation itself also would not have been much further in simulation time, so a comparison would not have been possible in a proper way.

Table 4.4.: Estimated values from plot 4.17,

model and time	C_m $[\mu N/W]$	standard deviation $\sigma(C_m)$ $[10^{-07}\ \mu N/W]$	$C_m/C_m(TTM)$
TTM	13.98	11.14	1.0
RES 100 ps	8.60	27.26	0.615
RES 125 ps	10.68	12.25	0.764
RES 150 ps	11.39	1.48	0.815

These examples show the possibility of hybrid simulations of TTM and NVE integration for a faster receiving of results. The NVE simulations were done on CPU (1), so the architecture provides poorer performance than the TTM simulation runs on CPU (2), but the simulations are as fast with regard to checkpoint file output as those on CPU (2). To find a proper time to start for NVE integration, the temperature distributions of the electronic and ionic system can be compared. This leads to results within the same order of magnitude as for TTM calculations. A threshold for the future should lie around 1 percent deviation between electron and ion temperature.

In figure 4.18 the time evolution of the specific impulse I_{sp} is given. It can be seen that it shows an increase that does not just flatten out over time from 140 ps on, but even decreases. No saturation value can be estimated from the calculation. This behaviour can be explained by the way the statistics were done in this case. Primarily, specific impulse and impulse coupling coefficient should show a similar behaviour due to their definitions:

$$I_{sp} = \frac{p_{plume}}{m\ g} \qquad\qquad c_m = \frac{p_{plume}}{E_{laser}}$$

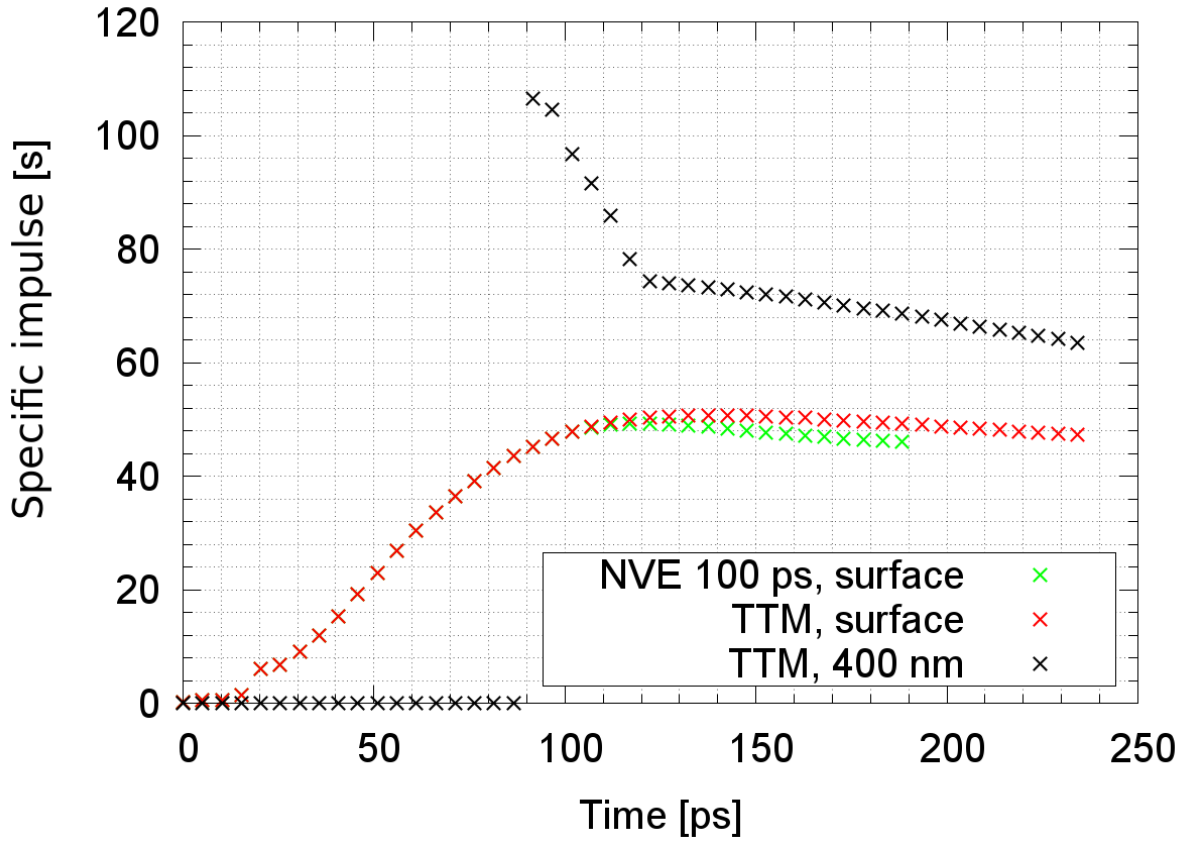

Figure 4.18.: Time evolution of specific impulse I_{sp} for simulation of laser pulse at 21 ps

Of coures, this is not the case because of their different nature. While in the formula of the impulse coupling coefficient the laser energy after some time becomes a constant - as it is assumed in the script - and so is the earths acceleration for the specific impulse, the mass of the plume is time dependent. The problem here is that after 140 ps from simulation start not only parts of the plume that is expelled from the surface

contribute to the statistics. Also slow particles of a mixture of liquid and gaseous aluminium belonging to the sample are added up. Of course, in this simulation times it is hard to distinguish between fluid aluminium that belongs to the plume and that recondensates on the surface. For calculation this means, even if the measured impulse increases, the specific impulse may decrease since the mass increase has more impact on the calculation than the impulse increase of the slower particles, resulting in higher denominators in the formula for I_{sp}.

If the x-value for statistics is set to 400 nm, however, still similar effects occur (cf. figure 4.18). The first measuring of values of course happens later than in surface case, since the particles first have to travel the additional distance of 400 nm. Then the statistics is dominated by just few particles, e.g. for the first value only 22 particles were taken into account. This leads to an overestimation of the specific impulse. When many particles have surpassed the 400 nm-mark, the slope of the time evolution becomes smoother. Due to the short simulation time, both the estimation curve for surface and higher distance do not come closer than about 9 s, but lie in the same order of magnitude.

The estimation of the specific impulse has to become more fine-tuned than stated here. Slow particle velocities within the thermal fluctuations for example should not be taken into account. Also the user has to look carefully at density plots for comparison. Maybe a better plume search algorithm can be implemented. However, it has been shown that in principal it is possible to estimate both aerospace parameters. These are compared to experimental data and VLL simulations later on.

The aerospace parameters can be compared on the basis that reflectivity plays a minor role and the Phipps model directly can be applied. In figure 4.19 the time evolution of impulse coupling coefficient and specific impulse at 2.1 ps from VLL data are plotted. They follow similar behaviours in time as IMD simulations. However, the values for $t \to \infty$ are higher than in IMD case. This simulation directly corresponds to the IMD parameters at $\sigma_t = 2.1$ ps. From the corresponding fits and the simulation at $\sigma_t = 21$ ps the values of table 4.5 are obtained. Also the IMD simulation outputs of c_m and I_{sp} are added with their errors, if fitting was possible. For 21 ps (first row) the specific impulse was a rule of thumb estimate from figure 4.17, therefore no calculated error is given.

In experiments with polymer and metal targets the Phipps formula was proven to estimate the aerospace parameters properly down to a lower limit of $t_{pulse} = 100$ ps

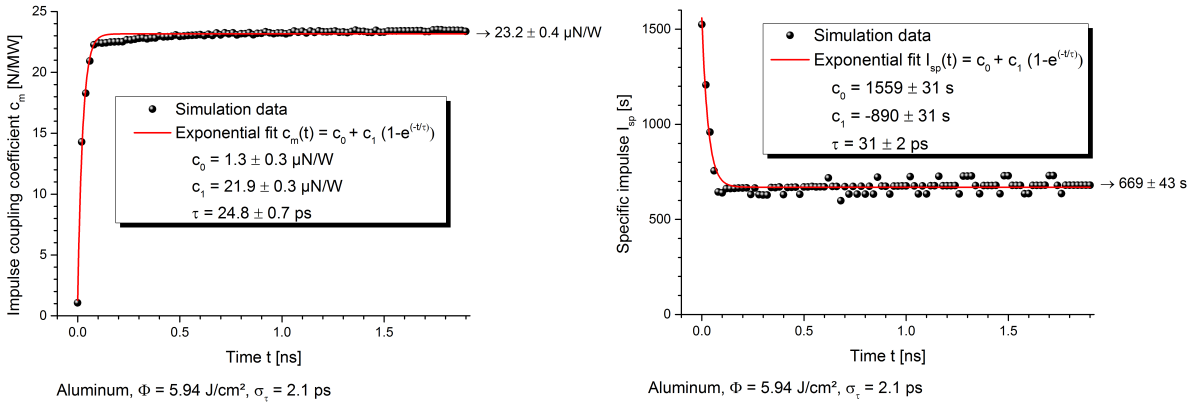

Figure 4.19.: Impulse coupling coefficient and specific impulse from VLL simulations, $\sigma_t = 2.1$ ps, [32]

($\sigma_t \approx 42.47$) [41]. Below that pulse duration it was proven to fail for polymers. The trend function formula for aluminium leads to an estimated value of [5]:

$$\begin{aligned} c_m\,[\mu N/W] &= \frac{55.6}{(\Phi\ \lambda\ \sqrt{\tau})^{0.301}} \\ &= \frac{55.6}{(2.998\ J/cm^2 \cdot 1.064\mu m \cdot \sqrt{500\ ps})^{0.301}} \\ \Rightarrow c_m &\approx 25\mu N/W \end{aligned}$$

As it can be seen from the estimated values for c_m, this model shows good comparison of simulations with IMD of aluminium for $\sigma_t = 21$ ps beside a factor of 2. However, these results have been obtained by just one simulation run, which is why they only can be treated as an estimate. Though plasma diagnostic of the ablation plume have already been undertaken in the laboratory [39], a detailed analysis of I_{sp} and c_m has not been possbile yet for the 500 ps-pulse laser at DLR.

Furthermore, the two simulation models show obvious differences in their estimations of impulse coupling coefficient and specific impulse. Both of course can only be compared to experimental results partially, since volume effects were not taken into account yet. With VLL this is not possible at all at present, while for IMD this is too time-consuming for craters of the present spatial extent, as will be shown in section 4.3. Moreover, IMD does not account for reflectivity changes, which might have a big influence in the picosecond pulse regime. Finally, the scripts for finding the pa-

Table 4.5.: Estimated values of aerospace parameters

simulation	C_m [$\mu N/W$]	standard deviation $\sigma(C_m)$ [$\mu N/W$]	I_{sp} [s]	standard deviation $\sigma(I_{sp})$ [s]
21 ps	14.0	11.1	~45	-
21 ps, VLL	25.0	0.1	435	3
2.1 ps	1.5	2.5	185	16
2.1 ps, VLL	23.2	0.4	669	43
210 ps, Phipps	24.98	-	-	-

rameters are incomplete and should be extended for proper estimates. A filtering of velocities has to be established for better estimation of the specific impulse.

Another possible parameter for comparison of experimental and simulation data except the aerospace parameters is the crater depth. In figure 4.20 on the left the surface elevation of an aluminium target after laser irradiation is given. Several fluences were applied in the laboratory, the pulse duration always was $t_{pulse} \approx 500$ ps ($\sigma_t \approx 210$ ps). The fit for crater depths was done with a Gaussian function. The estimation of the minimum and FWHM of these functions is plotted in figure 4.20 (right, in red and green). Also crater depths of homogeneous simulation with VLL are given by black points. It can be seen that the one dimensional hydrodynamic simulations overestimate the ablation depth by a factor of $2 - 2.8$. Additionally, two points represent IMD simulations at $\sigma_t = 21$ ps and $\sigma_t = 2.1$ ps, respectively. Under the assumption that the formula of Phipps 4.2 can be extended to that short pulses, these are equivalents to the DLR laser. They were determined by the distance measure from the liquid-solid interface to the initial surface. Initially the whole range of fluences was planned to get simulated, but due to the lack of time just these simulations were done, based on the laboratory laser at a fluence of $\sigma_e = 3$ J/cm². However, the points indicate that IMD predicts ablation depths in the correct order of magnitude. Also the problem here is that the simulation input of IMD and the experimental data can not be compared directly. As mentioned in the section before, reflectivity might play a big role in the shorter pulse range the two simulations belong to. True comparison can just be made by simulating a 210 ps pulse for a total simulation time of at least 1 ns, which takes almost half a year in simulation time on a standard work station. Since in the future experiments with shorter pulses might follow, the comparison will be much easier.

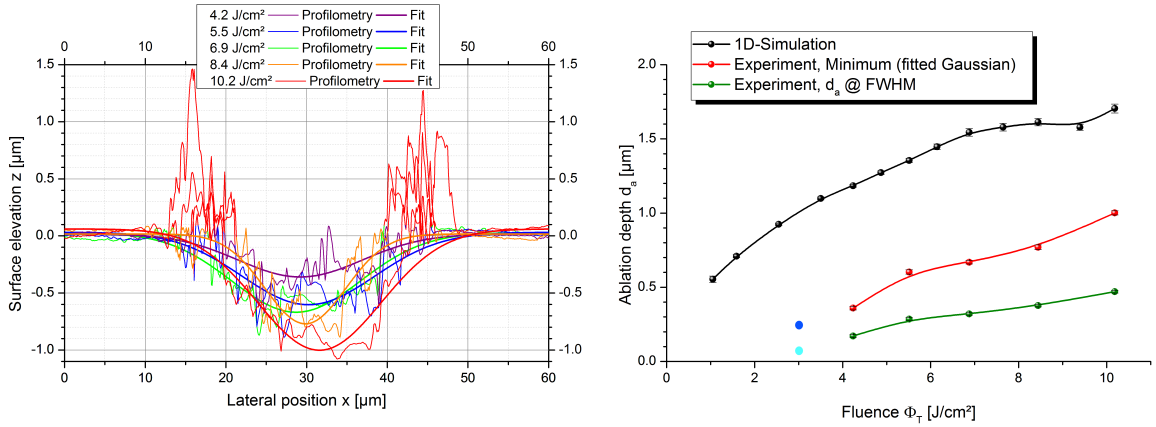

Figure 4.20.: An estimation of crater depths by Gaussian fits of experimental data (left) and in combination with VLL simulation output. The blue point refers to the IMD simulation of $\sigma_t = 21$ ps, the cyan point to the IMD simulation of $\sigma_t = 2.1$ ps (right) [39, 32].

4.3. Inhomogeneous irradiation

Homogeneous irradiation experiments were described in the previous sections due to the lack of computer power for a three-dimensional pulse resolution needed for comparison with craters formed by laboratory lasers. In this section a brief overview over possibilities is given. In figure 4.21 the time evolution of a three dimensional resolved laser pulse simulation is given from the first seven pictures. All of them were created with the open source visualization program **OVITO** [42], encoding follows their potential energy (red to white ⇔ bound to unbound ⇔ potential energy negative to zero). The last figure shows a cut through the sample which could be useful when checking for particle movement (encoding also follows the potential energy, but with a different color palette). For example, it would be interesting to investigate whether the observed crater edges are built by extrusion, i.e. the movement from the inner spot to the side, or if the main amount of edge particles is coming from expelled particles that fell back onto the surface.

However, real crater sizes with a diameter of $d \approx 20 - 100$ µm lie not within range at present. The example simulation shown here used a box with extents $x = 60.7$ nm, $y = 89.1$ nm and $z = 60.7$ nm. A simulation step of 250 fs plus output for each **.chkpt**-file took around 30 minutes. The laser pulse halfwidth was $\sigma_t = 100$ fs, the irradiation maximum at $t_0 = 230$ fs and the fluence set to 100926 J/m². In the parameter file four parameters for three dimensional positioning are given:

laser_tem_mode	1 0 0
laser_sigma_w_y	0.5
laser_sigma_w_z	0.5
laser_sigma_wo	150

The first parameter sets the laser spatial mode to Gaussian, the second and third give a relative position of the beam maximum to the box measures in y- and z-direction. The last parameter directly refers to the beam spot diameter ω_0 introduced in equation 3.7 (section 3.1.2). **laser_sigma_w_y** and **laser_sigma_w_z** can also be set to absolute values measured in Å when the parameters are bigger than 1. The reason for the sample being more extended in y-direction were initial thoughts on simulating overlap craters. However, this idea was not traced anymore since at this small scaling the crater depths and radii of craters are smaller than 3 nm, so predictions and statements can not be compared with real world values properly.

The irradiation region is much bigger than the crater it generates, which is not the case on µm scale. There the crater extents and irradiation area lay within the same order of magnitude.

As an extrapolation for needed storage and computing capacity a rough estimation is given. Ordinary crater depths during single pulse ablation in experiments lie around 1 µm. A sample of fitting depth 1.5 µm was already irradiated on ITAP's standard nodes ($\sigma_t = 21$ ps, cf. section 4.1), needing one day for the simulation of 2.97 ps. A sample with extents perpendicular to the irradiation direction of 20 µm x 20 µm with depth 2 µm would consist of

$$49380 \text{ x } 49380 \text{ x } 4938 \approx 12 \cdot 10^{12}$$

particles.

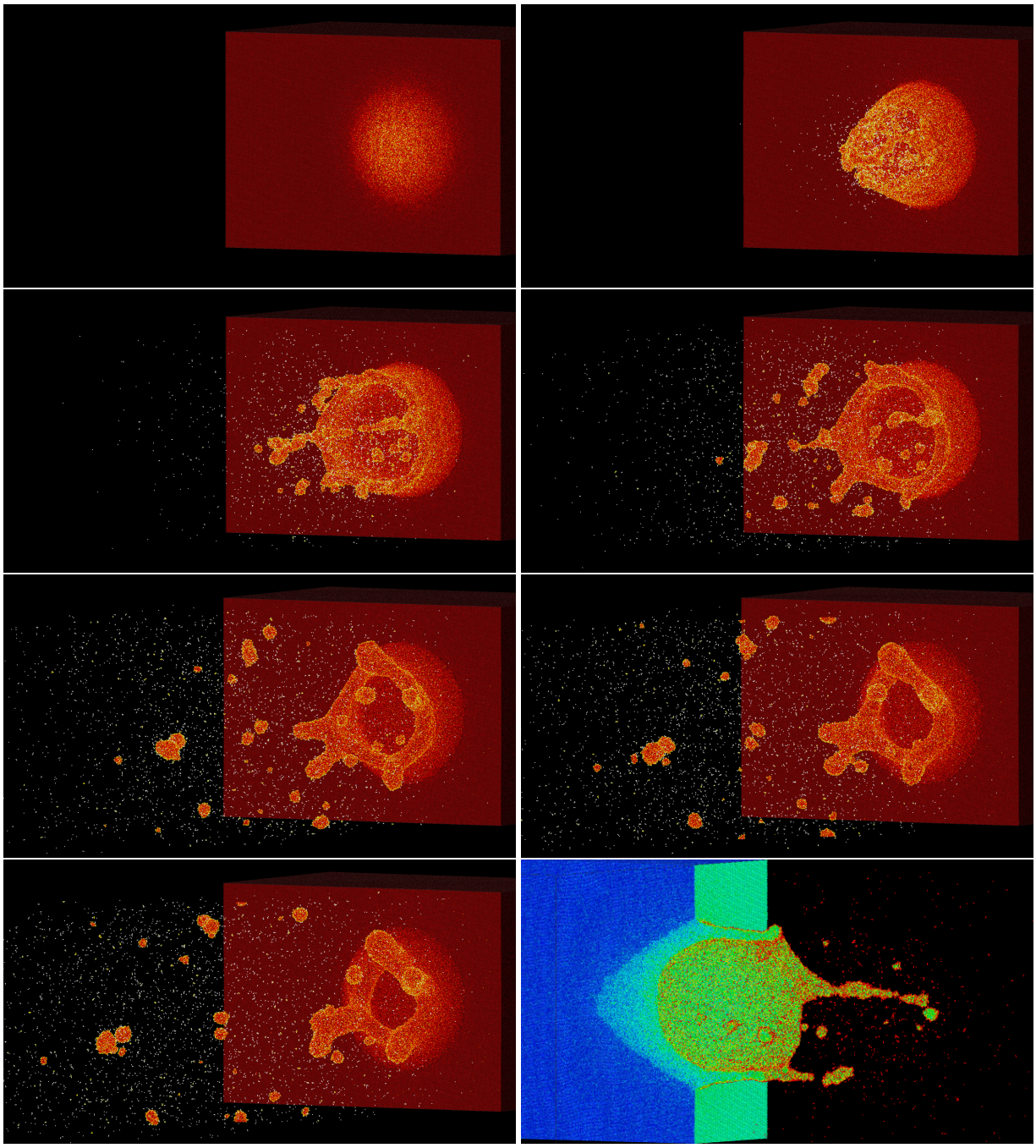

Figure 4.21.: Inhomogeneous RES simulation for (from left top to left bottom) $t_1 = 75$ fs, $t_2 = 1.225$ ps and $t_3 = 2.4$ ps, $t_4 = 3.375$ ps, $t_5 = 4.4$ ps and $t_6 = 4.6$ ps as well as $t_7 = 4.8$ ps, additionally an example of cutting for investigations on particle movements

5. Conclusions and outlook

The IMD code was shown to be usable in general for calculations of specific impulse and impulse coupling coefficient. Additional output can be provided by the software on atomistic scales and any parameter can be fine-tuned due to its open source coding. This also means that it is possible to change the code, which is necessary for the simulation of longer pulses. Also IMD simulations in general can be done with any material, as long as an EAM potential is available. The difficulty for other materials, e.g. gold, is to find a proper potential. No classification standard exists, each group develops its own potential appropriate for different issues.

The package IMD does not take into account for changes of optical properties due to laser irradiation and their effects on evolution of dynamic and optical values. However, this is a technical detail which should be solved first on further investigations and in principal is accessible. An relatively simple approach could be undertaken using an analytical function that is written into the code, following Drude or more detailed models. The time consumption in this case could lie in the range of a diploma thesis. Another starting point could be the implementation of the model used in VLL [28]. However, the model development and implementation would give rise to program another cell subsystem calculating optical properties. On one hand, this could also account for detailed description of electromagnetic waves, that can be splitted up into reflected, transmitted or reemitted parts, for example. On the other hand, the development is very time consuming and at minimum lies in the range of a PhD work.

The TTM parameters in IMD should be set more precisely, instead of simple power laws and constants. There exist calculations for electron-phonon coupling and electronic heat capacity which are tabulated [26] and then can be requested by the program for TTM boxes in which they shall be in effect.

Another problem with regard to the interface to PICLas code is the ionisation of particles due to high temperatures, which is not considered yet. The simulation of the

plume includes just neutral particles. Since heating takes place in non-thermal equilibrium, the Saha equation is not valid and ionisation can not be calculated that easily. However, in literature tables should exist that contain ionisation rates or proportions of ionisation grades at a certain temperature. These could be applied to TTM cells and written into Checkpoint files or PICLas output files as additional information for plasma plume simulations.

The provided output script for aerospace data gives rise to improvement. A first step is an additional filter to exclude atoms with a small velocity for better measurement of the specific impulse. However, the existing script results in a specific impulse that does not saturate in the given time scales, but only roughly can be estimated. The threshold velocity should lie within the order of thermal fluctuations.

It was shown that for three dimensional modelling in magnitudes comparable to experiments available computer systems and even supercomputers are not suitable yet. However, a scaling from 1 nm to 500 nm craters in diameter could be interesting. Sooner or later the ratio of depth to diameter might get similar to the behaviour in the dozen µm scale, as observed in the laboratory. Conclusions from simulations might be possible then to be connected to the real world.

Bibliography

[1] Workshop Mikroantriebe, 16./17.4.2013, Institut für technische Physik, DLR Stuttgart, `http://www.dlr.de/tp/Portaldata/39/Resources//Agenda.pdf`; visited at June 19, 2013. 1

[2] M. Armano, M. Benedetti, J. Bogenstahl, und D. Bortoluzzi. *LISA Pathfinder: the experiment and the route to LISA*. Classical and Quantum Gravity **26**, 094001 (2009). 1

[3] H. Dittus und T. van Zoest. *Applications of Microthrusters for Satellite Missions and Formation Flights Scenarios* **,AIP Conf. Proc. 1402**, 367–373 (2011). 1

[4] C. Ulrich. *Simulation der Laserablation an Metallen*. Diploma thesis, Universität Stuttgart (2007). 1, 3.1, 3.1.2, 3.1.3, 3.1.3

[5] C. R. Phipps und J. R. Luke. *Advantages of a ns-pulse micro-Laser Plasma Thruster*. AIP Conf. Proc. 664 S. 230–239 (2003). 2.1.1, 2.1.2, 4.2.3

[6] S. Karg, S. Scharring, und H.-A. Eckel. *Microthruster Research Activities at DLR Stuttgart - Status and Perspective* **,AIP Conf. Proc. 1402**, 374–382 (2011). 2.1

[7] E. Messerschmidt und S. Fasoulas. *Raumfahrtsysteme*. Fourth edition Auflage. Springer (2011). 2.1.2, 2.1.2

[8] M. Yazawa, C. Buttapeng, N. Harada, H. Suematsu, W. Jiang, und K. Yatsui. *Application to Space Propulsion with Ablation Plasma Produced by Pulsed Ion Beam*. Transactions of Space Technology Japan **3**, 1–6 (2005). 2.1.2

[9] Z. Zheng, J. Zhang, Y. Zhang, F. Liu, M. Chen, X. Lu, und Y. Li. *Enhancement of coupling coefficient of laser plasma propulsion by water confinement*. Applied Physics A **85**, 441–443 (2006). 2.1.2

[10] L. Myrabo, D. Messitt, und F. Mead. *Ground and flight tests of a laser propelled vehicle*. Aerospace Sciences Meetings (1998). 2.1.2

[11] I. Hertel und C. Schulz. *Atome, Moleküle und Optische Physik 2*. Springer (2010). 2.2

[12] Haken und H. Wolf. *Molekülphysik und Quantenchemie*. Physics and astronomy online library. Springer London, Limited (2006). 2.2, 2.2.1

[13] W. Demtröder. *Atome, Moleküle und Festkörper*. Experimentalphysik / Wolfgang Demtröder. Springer London, Limited (2005). 2.2, 2.2.1, 2.2.1, 2.3

[14] H. Ibach und H. Lèuth. *Solid-state Physics: An Introduction to Principles of Materials Science*. Advanced texts in physics. Springer (2009). 2.2, 2.2.2

[15] J. P. Gordon, H. J. Zeiger, und C. H. Townes. *The Maser—New Type of Microwave Amplifier, Frequency Standard, and Spectrometer*. Phys. Rev. **99**, 1264–1274 (Aug 1955). 2.3.1

[16] A. L. Schawlow und C. H. Townes. *Infrared and Optical Masers*. Phys. Rev. **112**, 1940–1949 (Dec 1958). 2.3.1

[17] T. H. Maiman. *Optical and Microwave-Optical Experiments in Ruby*. Phys. Rev. Lett. **4**, 564–566 (Jun 1960). 2.3.1

[18] T. W. Hänsch. *Repetitively Pulsed Tunable Dye Laser for High Resolution Spectroscopy*. Appl. Opt. **11**, 895–898 (Apr 1972). 2.3.1

[19] D. Frenkel und B. Smit. *Understanding molecular simulation: from algorithms to applications*. Computational Science Series, Vol 1. Academic Press (2002). 3.1

[20] F. Ercolessi und J. B. Adams. *Interatomic Potentials from First-Principles Calculations: The Force-Matching Method*. EPL (Europhysics Letters) **26**, 583 (1994). 3.1.1, 3.1, 4.1.1

[21] M. S. Daw und M. I. Baskes. *Embedded-atom method: Derivation and application to impurities, surfaces, and other defects in metals*. Phys. Rev. B **29**, 6443–6453 (Jun 1984). 3.1.1

[22] P. Brommer und F. Gähler. *Potfit: effective potentials from ab initio data*. Modelling and Simulation in Materials Science and Engineering **15**, 295 (2007). 3.1.1

[23] S. Sonntag. *Computer simulations of laser ablation from simple metals to complex metallic alloys*. Doktorarbeit, Universität Stuttgart (2011). 3.1.2, 3.1.3, 4.1.1, 4.1.1, 4.1.4

[24] D. S. Ivanov und L. V. Zhigilei. *Combined atomistic-continuum modeling of short-pulse laser melting and disintegration of metal films*. Phys. Rev. B **68**, 064114 (Aug 2003). 3.1.3

[25] S. Sonntag, J. Roth, und H.-R. Trebin. *Molecular Dynamics Simulations of Laser Induced Surface Melting in orthorhombic Al13Co4*. Applied Physics A (2010). 3.1.3

[26] Z. Lin, L. V. Zhigilei, und V. Celli. *Electron-phonon coupling and electron heat capacity of metals under conditions of strong electron-phonon nonequilibrium*. Phys. Rev. B **77** (2008). 3.1.3, 4.2, 5

[27] P. Chan, Y. Chan, und H. Ng. *Reflectivity of metals at high temperatures heated by pulsed laser*. Physics Letters A **61**, 151 – 153 (1977). 3.1.3

[28] M. E. Povarnitsyn, N. E. Andreev, P. R. Levashov, K. V. Khishchenko, und O. N. Rosmej. *Dynamics of thin metal foils irradiated by moderate-contrast high-intensity laser beams*. Phys. Plasmas 19 (2012). 3.2, 3.2.2, 5

[29] N. Andreev, M. Veisman, V. Efremov, und V. Fortov. *The Generation of a Dense Hot Plasma by Intense Subpicosecond Laser Pulses*. High Temperature **41**, 594–608 (2003). 3.2.1

[30] `http://vll.ihed.ras.ru`, Virtual Laser Lab; visited at June 10, 2013. 3.2.2

[31] J. Peter. *Validierung des PICLas-Codes als numerisches Verfahren zur Charakterisierung des Treibstrahls bei laser-ablativen Mikroantrieben*. Diploma thesis, unpublished, Universität Stuttgart (2013). 3.3, 3.3

[32] S. Scharring. *Post-processing and visualization of simulation data which have been obtained through the use of Virtual Laser Laboratory URL (http://vll.ihed.ras.ru), unpublished results (2013)* . 4, 4.15, 4.16, 4.19, 4.20

[33] D. Bäuerle. *Laser processing and chemistry*. Springer Berlin Heidelberg (2011). 4.2

[34] B. Hüttner und G. Rohr. *On the theory of ps and sub-ps laser pulse interaction with metals I. Surface temperature*. Applied Surface Science **103**, 269 – 274 (1996). 4.2

[35] C. Phipps, M. Birkan, W. Bohn, H.-A. Eckel, H. Horisawa, T. Lippert, M. Michaelis, Y. Rezunkov, A. Sasoh, W. Schall, . *Review: laser-ablation propulsion*. Journal of Propulsion and Power **26**, 609–637 (2010). 4.1.1

[36] D. Lide. *CRC Handbook of Chemistry and Physics ; 78th Edition 1997-1998*. CRC Press (1997). 4.1.3

[37] M. J. Assael, K. Kakosimos, R. M. Banish, J. Brillo, I. Egry, R. Brooks, P. N. Quested, K. C. Mills, A. Nagashima, Y. Sato, und W. A. Wakeham. *Reference Data for the Density and Viscosity of Liquid Aluminum and Liquid Iron*. Journal of Physical and Chemical Reference Data **35**, 285–300 (2006). 4.1.3

[38] G. Faussurier, C. Blancard, und P. L. Silvestrelli. *Evaluation of aluminum critical point using an ab initio variational approach*. Phys. Rev. B **79**, 134202 (Apr 2009). 4.1.3

[39] S. Karg und V. Fedotov. *Investigation of laser-ablative micropropulsion as an alternative thruster concept for precise satellite attitude and orbit control* (2013). ONERA-DLR Aerospace Symposium 2013, Palaiseau, France, May 27-29, 2013. 4.1.4, 4.2.3, 4.20

[40] J. Ihlemann, F. Beinhorn, H. Schmidt, K. Luther, und J. Troe. *Plasma and plume effects on UV laser ablation of polymers*. In *High-Power Laser Ablation 2004*, S. 572–580. International Society for Optics and Photonics (2004). 4.2.3

[41] `http://www.ovito.org`, OVITO - The open source visualisation tool ; visited at June 10, 2013. 4.3

A. Appendix

The Appendix includes detailed descriptions of self written scripts for the aerospace parameters and the interface to PICLas code. Brief descriptions of used programs follow. Finally, details on provided simulations are given.

A.1. Provided scripts

In principal all scripts developed are using the shell program **awk** to gather information and calculate values. It is a mighty tool when working on data in text files aligned in rows and columns.

Both scripts rely on a directory structure that follows

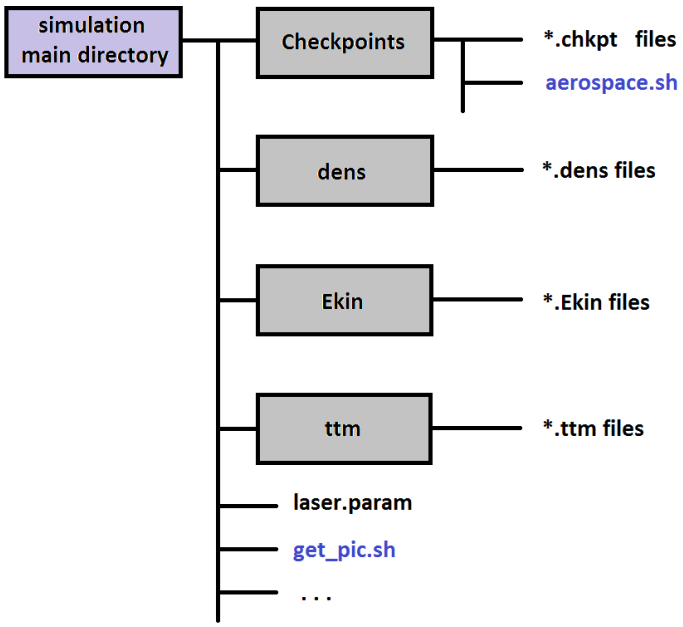

Boxes stand for named directories. The IMD parameter file **laser.param** contains

all simulation parameters like boundary conditions, integrator, laser parameters or damping. The directories contain files with output information of density, kinetic energy and TTM, as well as checkpoint files including all particle positions, velocities and potential energies. The script **aerospace.sh** is given in section A.1.1, **get_pic.sh** in section A.1.2.

A.1.1. Main parameters for aerospace engineering

```
#/bin/bash

LC_NUMERIC=C
LC_COLLATE=C

printf "timestep \t c_m \t\t I_sp  \t\t fluence \t area \t\t
   pulse_energy\n" > DLR.data

##### Summation of columns 3 / 3*4 / 3*5 / 3*6 = masses / p_x / p_y /
   p_z #####
for file in *.chkpt

do
        awk 'NR>8 {if ($4<0)  sumx += $7*$3*1000/1.018 } END {printf "%f
            ", sumx }' < $file >> velocities_$file.dat
        awk 'NR>8 {if ($4<0)  sumy += $8*$3*1000/1.018 } END {printf "%f
            ", sumy }' < $file >> velocities_$file.dat
        awk 'NR>8 {if ($4<0)  sumz += $9*$3*1000/1.018 } END {printf "%f
            ", sumz }' < $file >> velocities_$file.dat
        awk 'NR>8 {if ($4<0)  summass += $3 } END {printf "%f ", summass
            }' < $file >> velocities_$file.dat
done

##### Length calculation of velocity vector #####

for file in *.chkpt
do
        awk '{ pabsolute = ($2*$2 + $3*$3 + $1*$1)**(1/2) } END {printf
           "%f ", pabsolute }' < velocities_$file.dat >>velocities_$file
           .dat
done
```

```
##### Get area and fluence #####
for file in *.chkpt

do
   awk '{if (NR==4) printf "%f ",$3}' < $file >> velocities_$file.dat
   awk '{if (NR==5) printf "%f ",$4}' < $file >> velocities_$file.dat
   awk '{if (index($0,"laser_sigma_e")==1) printf "%f \n",$2*16.02}' <
      ../laser.param >> velocities_$file.dat
done

##### Get direction vector of impulse #####
for file in *.dat

do
        read -r  p_x p_y p_z mass p_abs a_x a_y fluence < $file

        printf "%g \t %g \t %g \t%g \t\t %g \t\t %g \t %g \t %g" $p_x
           $p_y $p_z $mass $p_abs $a_x $a_y $fluence >> $file
        printf "\n p_x [m/s*amu]\t p_y [m/s*amu]\t p_z [m/s*amu]\tmass [
           amu]\t p_absolute [m/s*amu] \t x_dir [A] \t y_dir [A] \t
           fluence [J/m^2]\n\n" >> $file

        echo "direction vector coordinates (scaling):" >> $file
        X=$(echo "100*$p_x/$p_abs" | bc -l)
        Y=$(echo "100*$p_y/$p_abs" | bc -l)
        Z=$(echo "100*$p_z/$p_abs" | bc -l)
        printf "X\t%g\n" $X >> $file
        printf "Y\t%g\n" $Y >> $file
        printf "Z\t%g\n\n" $Z >> $file

##### Calculate C_m, I_sp, timestep, area, fluence and energy, then
   print to files <>.dat and ../DLR.data #####
        C=$(echo "$p_abs/$a_x/$a_y/$fluence*0.00000016605" | bc -l)
        TIME=$(echo $file | sed "s/[^0-9]//g")
        I=$(echo "$p_abs/$mass/9.81" | bc -l)
        A=$(echo "$a_x*$a_y" | bc -l)
        ENERGY=$(echo "$a_x*$a_y*$fluence" | bc -l)

        printf "Specific Impulse Isp [second]\n%g\n" $I >> $file
        printf "Coupling Coefficient [kg m / J s]\n%g\n" $C >> $file

        echo "##### above showing file $file #####" >> $file
```

```
        printf "%g \t\t %g \t %g \t %g \t\t %g \t %g\n" $TIME $C $I
           $fluence $A $ENERGY>> DLR.data
done
```

A.1.2. Interface to PICLas

```
#/bin/bash

LC_NUMERIC=C
LC_COLLATE=C

# USAGE: sh get_PIC.sh <line of surface cell (get from laser.0.dens by
   hand)> <begin of statistics (absolute value of dist_ll x)> <beginning
    of sample in Angstrom (get from Checkpoint file, first particle)>

mkdir to_PICLas

XMAXLINE=$(($1-1))
XMAX=$(echo "($2+$3)/10" | bc -l)
XSTEP=$(echo "$XMAX/$XMAXLINE" | bc -l)

echo $XMAXLINE
echo $XMAX
echo $XSTEP

for file in ttm/laser.*.ttm
do
  TIME=$(echo $file | sed "s/[^0-9]//g")
  TIME2=$(($TIME/10))
  printf "# File contains distribution of temperature and density for
     whole simulation box at $TIME2 ps\n" > to_PICLas/to_PICLas_$TIME.
     dat
  printf "# In distance from x= 0 nm to x= %f nm in front of the sample\
     n" $XMAX  >> to_PICLas/to_PICLas_$TIME.dat
  printf "# x_l (nm) \t x_r (nm) \t rho (g/cm^3) \t T_ion (K)\n" >>
     to_PICLas/to_PICLas_$TIME.dat
  LINE=8
  echo $TIME
  echo $XMAXLINE
  while [ $LINE -le $XMAXLINE ]
  do
```

```
    Xl=$(echo "($LINE-8)*$XSTEP" | bc -l)
    Xr=$(echo "($LINE-8)*$XSTEP+$XSTEP" | bc -l)
    printf "%6.6f \t" $Xl >> to_PICLas/to_PICLas_$TIME.dat
    printf "%6.6f \t" $Xr >> to_PICLas/to_PICLas_$TIME.dat
    awk -v cell=$LINE '{if (NR==cell) printf "%6.8f \t",$1*44.1537}' <
       dens/laser.$TIME.dens >> to_PICLas/to_PICLas_$TIME.dat
    awk -v cell=$LINE '{if (NR==cell) printf "%6.8f \n",$1*11605}' <
       Ekin/laser.$TIME.Ekin >> to_PICLas/to_PICLas_$TIME.dat
  LINE=`expr $LINE + 1`
  done
done
```

A.2. Simulational details

Laser parameters of simulations followed table A.1.

Table A.1.: Laser parameters of all provided simulations

naming	pulse duration t_{FWHM} [ps]	σ_t [ps]	σ_e [J/m²]	total simulation time [ps]
100 fs	0.2397	0.102	10.01	50.9
200 fs	0.4794	0.204	20.03	50.9
500 fs	1.1986	0.509	50.06	50.9
1 ps	1.2972	1.018	100.13	55.99
5 ps	11.986	5.090	500.62	55.99
10 ps	23.972	10.180	1001.25	RES 122.1 TTM 66.1
50 ps	119.86	50.900	5006.25	RES 142.5 TTM 234.1
100 ps	239.72	101.800	10012.50	RES 590.4 TTM 483.5
DLR laser	500	213.147	30000	-
210 ps	503.41	213.780	29989.44	RES 45.5 TTM 323.6
21 ps	50.341	21.378	9491.05	RES 132.9 TTM 236.7
2.1 ps	5.0341	2.138	2998.94	TTM 36.9
210 fs	0.5034	0.214	949.10	TTM 38.7